

Wing Leading Edge Joint Laminar Flow Tests

Aaron Drake, Russell V. Westphal
Washington State University, Tri-Cities, Richland, Washington

Fanny A. Zuniga, Robert A. Kennelly, Jr., Dennis J. Koga
Ames Research Center, Moffett Field, California

October 1996



National Aeronautics and
Space Administration

Ames Research Center
Moffett Field, California 94035-1000

Wing Leading Edge Joint Laminar Flow Tests

AARON DRAKE,* RUSSELL V. WESTPHAL,* FANNY A. ZUNIGA, ROBERT A. KENNELLY, JR.,
and DENNIS J. KOGA

Ames Research Center

Summary

An F-104G aircraft at NASA's Dryden Flight Research Center has been equipped with a specially designed and instrumented test fixture to simulate surface imperfections of the type likely to be present near the leading edge on the wings of some laminar flow aircraft. The simulated imperfections consisted of five combinations of spanwise steps and gaps of various sizes. The unswept fixture yielded a pressure distribution similar to that of some laminar flow airfoils. The experiment was conducted at cruise conditions typical for business jets and light transports: Mach numbers were in the range 0.5–0.8, and unit Reynolds numbers were 1.5–2.5 million per foot. Skin friction measurements indicated that laminar flow was often maintained for some distance downstream of the surface imperfections. Further work is needed to more precisely define transition location and to extend the experiments to swept-wing conditions and a broader range of imperfection geometries.

Nomenclature

a	local sound speed (ft/s)
c	chord (ft)
C_f	local skin friction coefficient ($\tau/(0.5 \cdot \rho \cdot U^2)$)
$C_{f1,2,4}$	skin friction coefficient at gauges 1, 2 and 4, respectively
C_p	coefficient of pressure ($(p-p_\infty)/q_\infty$)
FTF	flight test fixture
h	Stanton gauge height (in)
h_p	altitude (ft)
HLFC	hybrid laminar flow control
M_∞	free-stream Mach number

NLF	natural laminar flow
p	local static pressure (lb/ft ²)
p_∞	free-stream static pressure (lb/ft ²)
P_o	total pressure (lb/ft ²)
q_∞	free-stream dynamic pressure (lb/ft ²)
Re/ft	unit Reynolds number ($\rho_\infty \cdot U_\infty / \mu_\infty$)
U	local velocity outside boundary layer (ft/s)
U_∞	free-stream velocity (ft/s)
x	chordwise distance from nose leading edge (in)
x_{tr}	chordwise distance from leading edge to transition location (in)
z	spanwise distance from FTF root (in)
α	angle-of-attack (degrees)
β	side-slip angle (degrees)
ΔP	Stanton gauge pressure difference (lb/ft ²)
μ_∞	freestream viscosity (sl/ft*s)
ρ	local density (sl/ft ³)
ρ_∞	freestream density (sl/ft ³)
τ	skin friction (lb/ft ²)

Motivation

The competitive pressure to build more energy-efficient aircraft has generated a considerable amount of research aimed at achieving natural laminar flow (NLF) and hybrid laminar flow control (HLFC) on transonic aircraft wings to reduce skin friction drag. This research has focused primarily on airfoil design and understanding transition behavior with less concern for the surface imperfections and manufacturing variations inherent to production aircraft (ref. 1). Well-defined

* Washington State University, Tri-Cities,
Richland, WA 99352-1643

criteria in such areas as allowable sizes of gaps and steps that result from aircraft skin seams, as well as criteria for rivet and fastener sizes are essential if NLF/HLFC technology is to be incorporated on mass-produced aircraft.

Most business jet wings are constructed with a spanwise joint between the leading-edge-skin piece and the main-wing skin approximately four to six inches downstream of the leading edge (see fig. 1). The leading-edge-skin piece on business jets is typically polished aluminum and is intended to be removable for (infrequent) structural inspections. A major obstacle to constructing a wing which will achieve laminar flow is the attachment of the leading-edge piece (see fig. 2(a)). A proposed method which is very similar to current business jet practices, involves milling out a strip on the leading edge adjacent to the joint where the screws would attach. This would then be covered by a plastic or aluminum strip held in place by adhesive. This strip would cover the joint gap and be nearly flush with the wing surface (see fig. 2(b)). The cover strip could easily be trimmed to minimize the resulting gaps and step misalignment.

Before the proposed construction method can be used, it is necessary to have an understanding of the allowable size of steps and gaps that are needed to permit laminar flow. This experiment begins to answer the question: how small do steps and gaps in the surface of business jet type aircraft wings need to be to allow laminar flow? To do this, a simulated wing leading edge was constructed that would allow configurations with various size steps and gaps to be tested in the presence of a wing-like pressure distribution.

Experiment

To address concerns over scale effects and maximize the applicability of the results obtained, this experiment was conducted in flight using a full scale test article. A facility ideally suited to such experimentation is the Dryden Flight Research Facility F-104 Flight Test Fixture (ref. 2). The Flight Test Fixture (FTF) is a low aspect ratio ventral fin mounted on an F-104G aircraft (see fig. 3). The FTF has a span of 2 ft and an approximate chord of 7 ft. The size of the FTF and the operational envelope of the F-104 allow full scale testing directly applicable to business jets and light transports. Furthermore, the flight envelope of the F-104/FTF allows speed, altitude, Mach number, Reynolds number, and any atmospheric effects to be duplicated precisely. However, the key advantage to conducting this experiment in flight, as opposed to ground-based test-

ing using a wind tunnel, is the ability to precisely match the disturbance environment of the test to that which would be encountered in practice.

In order to perform NLF experiments using the FTF, it is necessary to have a noseshape whose pressure distribution is similar to that of an NLF airfoil. In this way, the flow over the wing leading-edge region of the aircraft can be simulated on the noseshape of the FTF. Since no suitable noseshape existed, a replacement was designed (see fig. 4). The primary goal of this design was to provide a pressure distribution similar to that found on some recently designed laminar flow airfoils (ref. 3). These airfoils are characterized by smoothly accelerating pressure gradients over the upstream 25% of chord. Additionally, it was desirable to minimize the sensitivity of the design to small changes in angle of attack. Angle of attack on the FTF corresponds to aircraft sideslip and cannot be assumed to be precisely constant in flight. For this design, it was assumed that sideslip could be controlled to within $\pm 0.5^\circ$. To allow an appropriate error margin, the pressure distribution on the fixture was to remain well-behaved at up to 1.5° angle of attack. The flow about the final shape, denoted TFN-7525 (see table 1), was analyzed using the two-dimensional full-potential CFD code for a range of conditions (ref. 4). The results showed that TFN-7525 met all the design goals. A favorable pressure gradient is maintained over the first 80% of the noseshape and remains favorable throughout the range of angle-of-attack and Mach number examined. Figures 5 and 6 show and tabulate the pressure distributions actually measured in flight.

To allow different configurations of surface discontinuities to be examined, several aluminum strips were milled. These strips, or coverpieces, fit into the spanwise slot on the left side of the noseshape. By using cover-pieces of different widths and thicknesses, a variety of possible surface configurations could be tested. Five configurations were chosen as representative and were denoted with letters A through E (see fig. 7). Configuration A consisted of two 0.06 in. gaps and a 0.02 in. step. Configuration B consisted of a single 0.03 in. gap with no step. Configuration C was similar to configuration A but without the step. Configuration D consists of a single 0.13 in. gap with no step. Configuration E was designed to be identical to D except that the downstream lip of the gap was rounded rather than square. Work by other researchers has indicated that rounded corners on surface discontinuities decreases their tendency to trip the boundary layer (ref. 5).

The noseshape was instrumented with a single chordwise row of pressure taps located approximately halfway between the fixture root and tip (see fig. 8). This row of pressure taps wrapped around the leading edge providing pressure distributions on both sides of the nose. A comparison of these pressure distributions was used to ensure that the fixture angle of attack (aircraft side-slip) stayed near zero. To determine boundary layer state, hot-film gauges and Stanton gauges were used. The arrangement of these gauges was chosen to unambiguously determine if the boundary layer was tripped at or near the surface discontinuities (rather than the precise location of the transition front).

The Stanton gauge is a simple, effective method for measuring skin friction. The Stanton gauges were formed by placing segments of razor blades over a static pressure taps to form a kind of flattened total pressure tube (ref. 6). The sloped cutting edge of the blade forms the upper wall of the tube, and the surface forms the lower wall (see fig. 9). The blade faces directly upstream and the tip was aligned directly over the forward-most lip of the pressure tap. To obtain a skin friction measurement with the Stanton gauge, the difference between the gauge pressure and the local static pressure must be obtained. This was accomplished by having a static tap located adjacent to the Stanton gauge at the same chordwise location and just far enough away to prevent interference in the measured static pressure from the razor blade. The flow over the noseshape was assumed to be two-dimensional.

Skin friction was determined by applying East's calibration to the pressure difference (ΔP) measured by the Stanton gauge (ref. 7). East's calibration relates two dimensionless quantities,

$$x^* = \log \left\{ \frac{\Delta \bar{P} \cdot h^2 \cdot \rho}{\mu^2} \right\}$$

$$y^* = \log \left\{ \frac{\bar{\tau} \cdot h^2 \cdot \rho}{\mu^2} \right\}$$

where h is the gage height.

The first of these quantities (x^*) can be determined by knowing the Stanton-gauge-pressure difference, the

flow properties and the gauge geometry. Using the calibration relation,

$$y^* = -0.23 + 0.618 \cdot x^* + 0.0165 \cdot (x^*)^2$$

the value of the second dimensionless quantity (y^*) can be determined. Once the value of y^* has been found, the same flow properties and gauge geometry information can be used to solve for the skin friction (τ). Because the calibration relation uses the flow properties, the exact relation between skin friction and Stanton-gauge-pressure difference is different for each flight condition. The large changes in skin friction associated with boundary layer transition result in large, easily identifiable changes in the Stanton-gauge-pressure difference.

Despite the fact that East's calibration was made for a turbulent boundary layer, as long as the razor blade is sized correctly, it should be valid with 20% accuracy in laminar boundary layers (ref. 8). The razor blade was sized so that it lay completely within the boundary layer for both laminar and turbulent boundary layers. East's calibration does require that the proportions of the razor blade strictly adhere to those used in the initial calibration. Four Stanton gauges were placed downstream of the coverpiece, each at one of two chordwise locations. Gauges number 2 and 3 were placed immediately downstream of the coverpiece and gauges 1 and 4 were placed further downstream. A small trip strip was placed just downstream of the coverpiece directly in front of gauge 1 so that the reading from gauge 1 could be used as a known turbulent signal.

Five hot-film gauges were also placed on the nose-shape. These were located adjacent to the Stanton gauges with the fifth one just upstream of the coverpiece, in front of the trip strip for gauge 1. The results of the hot films are presented in Zuniga et al. (ref. 9).

A range of target test conditions was chosen based on the typical cruise operating conditions of business jets and light transports. Mach numbers were varied between 0.50 and 0.80 in increments of 0.10 and two Reynolds numbers were selected: 1.50×10^6 and 2.5×10^6 per foot. The actual test points varied somewhat from the target values, being affected by operational limitations and weather conditions.

Results

During the first flight, it was discovered that gauge 3 was malfunctioning; it was not possible to correct this problem. As a result only three working gauges could be used: gauge 1 was located at $x = 11.5$ in. and because of the presence of a trip strip, provided a known turbulent signal. Gauge 2 was located at $x = 5.5$ in. and measured the skin friction approximately half an inch downstream of the aft edge of the coverpiece. Gauge 4, located at $x = 11.5$ in., provided a measurement six-and-a-half inches downstream of the coverpiece. By comparing the C_{fs} measured at these three locations it was possible to determine if the boundary layer was laminar or turbulent at each location (see table 2 and figs. 10–15).

Because of the arrangement of the Stanton gauges, it was not possible to determine the exact location of transition. Rather, it could only be said that transition occurred in one of three regions: 1) $X_{tr} < 5.5$ in.—if both the forward and the downstream Stanton gauge indicated turbulent flow the transition location was either on the coverpiece or immediately downstream of it, 2) 5.5 in. $< X_{tr} < 11.5$ in.—if the forward gauge indicated laminar flow and the downstream gauge indicated turbulent, and 3) $X_{tr} > 11.5$ in.—if both gauges indicated laminar flow, transition must have occurred aft of all the gauges.

Because of the limited number of flights, most configurations could only be tested on a single flight. As a result, it was not possible to test more than twelve conditions for any one configuration, and for most configurations the number of conditions tested was less than this. The boundary layer was observed to remain laminar downstream of the coverpiece at a total of 29 of the 46 different conditions tested; at many of these conditions the forward gauge identified a laminar boundary layer and the downstream gauge measured turbulent. The location of boundary layer transition was clearly dependent on the coverpiece configuration.

Comparisons between configurations generally show that as qualitatively expected, the smaller the discontinuities in the surface, the higher the Reynolds number at which the boundary layer is observed to be turbulent (see figs. 16–20).

From the data obtained, it is not clear that the transition location was dependent on Mach number. However, for configurations B and D the results show a possible influence of Mach number. With configuration B, at approximately $Re = 2.0 \times 10^6$ /ft, the boundary layer remained laminar past the aft gauge for all Mach numbers except the highest, $M = 0.8$. At this condition, the aft gauge indicated a turbulent boundary layer. However, it is not clear that this must be due to the effects of Mach number since the Reynolds number at this condition was also slightly higher than the others. A similar situation occurred for configuration D at a nominal Reynolds number of 1.5×10^6 /ft.

A comparison of the results of configurations D and E show that there may be some beneficial effects from rounding the edge, as in configuration E. However, due to the sparseness of the data, any such benefits cannot be determined absolutely.

Despite the fact that the data points examined are rather sparse and the number of step and gap configurations limited, a beginning has been made at understanding the effects of steps and gaps in aircraft surfaces on boundary layer transition. Further work should include an attempt to more precisely measure the transition location in order to better understand the effects of changes in Mach and Reynolds numbers. Additionally, all work done here was with an unswept leading edge, whereas many aircraft of the type for which one might consider NLF or HLFC designs have swept wings. Many of the techniques used in this experiment could be applied to a test with a swept leading edge. Such a test could make use of Stanton gauges for skin friction measurements with confidence. Most importantly, this experiment is only a starting point for comprehensive research aimed at not only quantifying the allowable step and gap sizes, but at an understanding of the phenomena that create these limits.

References

1. Drake, Aaron; and Kennelly, Robert A., Jr.: Selected Experiments in Laminar Flow: An Annotated Bibliography. NASA TM-103989, December 1992.
2. Meyer, Robert R., Jr.: A Unique Flight Test Facility: Description and Results. NASA TM-84900, 1982.
3. Campbell, R. L.; Waggoner, E. G.; and Phillips, P. S.: Design of a Natural Laminar Flow Wing for a Transonic Corporate Transport. AIAA Paper 86-0314, 1986.
4. Kennelly, Robert A., Jr.: Improved Method for Transonic Airfoil Design-by-Optimization. AIAA paper 83-1864, 1983.
5. Holmes, B. J.; and Obara, C. J.: Observations and Implications of Natural Laminar Flow on Practical Airplane Surfaces. NASA TP-2256, 1984.
6. Hool, J. N.: Measurement of Skin Friction Using Surface Tubes. Aircraft Engineering, vol. 28, 1956.
7. East, L. F.: Measurement of Skin Friction at Low Subsonic Speeds by the Razor-Blade Technique. Aero. Res. Coun. London, R&M 3525, 1966.
8. Bradshaw, P.; and Gregory, N.: The Determination of Local Turbulent Skin Friction from Observation in the Viscous Sub-layer. Aero. Res. Coun. London, R&M 3202, 1961.
9. Zuniga, Fanny A.; Drake, Aaron; Kennelly, Robert A., Jr.; Koga, Dennis J.; and Westphal, Russell V.: Transonic Flight Tests of a Laminar Flow Leading Edge with Surface Excrescences. NASA TM-4597, August 1994. Also presented as AIAA Paper 94-2142, Colorado Springs, Colorado, June 1994.

Table 1. Symmetric noseshape surface coordinates

x (in.)	y (in.)	x (in.)	y (in.)
0.000	0.000	7.756	2.773
0.152	0.408	7.908	2.795
0.304	0.577	8.060	2.816
0.456	0.706	8.212	2.837
0.608	0.815	8.364	2.858
0.760	0.912	8.516	2.878
0.912	0.999	8.668	2.898
1.064	1.079	8.820	2.917
1.217	1.153	8.972	2.937
1.369	1.223	9.124	2.955
1.521	1.289	9.276	2.974
1.673	1.352	9.428	2.991
1.825	1.412	9.580	3.009
1.977	1.468	9.733	3.026
2.129	1.523	9.885	3.043
2.281	1.575	10.037	3.059
2.433	1.625	10.189	3.075
2.585	1.674	10.341	3.090
2.737	1.722	10.493	3.105
2.889	1.768	10.645	3.120
3.041	1.812	10.797	3.134
3.193	1.856	10.949	3.148
3.346	1.898	11.101	3.161
3.498	1.939	11.253	3.174
3.650	1.978	11.405	3.186
3.802	2.017	11.557	3.198
3.954	2.054	11.709	3.210
4.106	2.091	11.862	3.221
4.258	2.127	12.014	3.231
4.410	2.162	12.166	3.242
4.562	2.196	12.318	3.251
4.714	2.229	12.470	3.261
4.866	2.262	12.622	3.270
5.018	2.294	12.774	3.278
5.170	2.325	12.926	3.286
5.322	2.356	13.078	3.294
5.475	2.386	13.230	3.301
5.627	2.415	13.382	3.308

Table 1. Concluded

5.779	2.444	13.534	3.314
5.931	2.473	13.686	3.320
6.083	2.501	13.838	3.325
6.235	2.528	13.991	3.330
6.387	2.555	14.143	3.333
6.539	2.581	14.295	3.337
6.691	2.607	14.447	3.340
6.843	2.632	14.599	3.342
6.995	2.656	14.751	3.344
7.147	2.681	14.903	3.345
7.299	2.704	15.055	3.347
7.451	2.728	15.270	3.347
7.604	2.750		

Table 2. Matrix of the 46 test conditions

Point	Config.	Ma	Re/ft	C _{f2}	C _{f1}	C _{f4}	x _{tr} (in.)
1a	A	0.742	1.57 x 10 ⁶	0.00097	0.00294	0.00320	5.5–11.5
1b	A	0.699	1.53 x 10 ⁶	0.00106	0.00298	0.00325	5.5–11.5
1c	A	0.592	1.45 x 10 ⁶	0.00105	0.00299	0.00327	5.5–11.5
1d	A	0.806	2.44 x 10 ⁶	0.00433	0.00326	0.00360	0.0–5.5
1e	A	0.743	2.40 x 10 ⁶	0.00488	0.00315	0.00338	0.0–5.5
1f	A	0.711	2.42 x 10 ⁶	0.00461	0.00307	0.00327	0.0–5.5
1g	A	0.580	2.33 x 10 ⁶	0.00459	0.00305	0.00326	0.0–5.5
1h	A	0.491	2.34 x 10 ⁶	0.00450	0.00303	0.00322	0.0–5.5
2a	B	0.775	1.47 x 10 ⁶	0.00178	0.00324	0.00096	11.5–
2b	B	0.747	1.55 x 10 ⁶	0.00162	0.00308	0.00126	11.5–
2c	B	0.800	2.03 x 10 ⁶	0.00175	0.00320	0.00435	5.5–11.5
2d	B	0.748	1.99 x 10 ⁶	0.00158	0.00314	0.00209	11.5–
2e	B	0.599	1.52 x 10 ⁶	0.00154	0.00319	0.00097	11.5–
2f	B	0.698	1.99 x 10 ⁶	0.00149	0.00310	0.00231	11.5–
2g	B	0.798	2.50 x 10 ⁶	0.00242	0.00324	0.00356	5.5–11.5
2h	B	0.751	2.52 x 10 ⁶	0.00169	0.00314	0.00363	5.5–11.5
2i	B	0.597	1.98 x 10 ⁶	0.00141	0.00312	0.00238	11.5–
3a	B	0.599	1.52 x 10 ⁶	0.00142	0.00306	0.00165	11.5–
3b	B	0.701	2.51 x 10 ⁶	0.00140	0.00315	0.00377	5.5–11.5
3c	B	0.599	2.52 x 10 ⁶	0.00134	0.00307	0.00396	5.5–11.5
4a	C	0.799	1.57 x 10 ⁶	0.00166	0.00333	0.00407	5.5–11.5
4b	C	0.695	1.51 x 10 ⁶	0.00145	0.00317	0.00397	5.5–11.5

Table 2. Concluded

4c	C	0.799	2.03×10^6	0.00185	0.00353	0.00391	5.5–11.5
4d	C	0.704	2.00×10^6	0.00153	0.00334	0.00402	5.5–11.5
4e	C	0.801	2.44×10^6	0.00330	0.00355	0.00371	5.5–11.5
4f	C	0.699	2.52×10^6	0.00163	0.00324	0.00366	5.5–11.5
4g	C	0.599	2.52×10^6	0.00142	0.00316	0.00362	5.5–11.5
4h	C	0.605	2.02×10^6	0.00141	0.00325	0.00379	5.5–11.5
4i	C	0.505	2.03×10^6	0.00166	0.00323	0.00393	5.5–11.5
4j	C	0.499	2.47×10^6	0.00411	0.00316	0.00349	0.0–5.5
5a	D	0.800	1.54×10^6	0.00533	0.00330	0.00308	0.0–5.5
5b	D	0.693	1.46×10^6	0.00184	0.00312	0.00356	5.5–11.5
5c	D	0.595	1.51×10^6	0.00296	0.00307	0.00350	5.5–11.5
5d	D	0.697	2.00×10^6	0.00466	0.00323	0.00319	0.0–5.5
5e	D	0.690	2.48×10^6	0.00462	0.00322	0.00320	0.0–5.5
5f	D	0.599	2.51×10^6	0.00446	0.00318	0.00324	0.0–5.5
6a	E	0.800	1.49×10^6	0.00259	0.00367	0.00364	5.5–11.5
6b	E	0.707	1.53×10^6	0.00184	0.00325	0.00334	5.5–11.5
6c	E	0.806	2.08×10^6	0.00522	0.00340	0.00325	0.0–5.5
6d	E	0.733	2.08×10^6	0.00478	0.00327	0.00324	0.0–5.5
6e	E	0.798	2.51×10^6	0.00512	0.00347	0.00328	0.0–5.5
6f	E	0.508	1.54×10^6	0.00220	0.00311	0.00322	5.5–11.5
6g	E	0.596	1.97×10^6	0.00433	0.00319	0.00331	0.0–5.5
6h	E	0.601	2.54×10^6	0.00441	0.00315	0.00317	0.0–5.5
6i	E	0.503	2.02×10^6	0.00466	0.00318	0.00330	0.0–5.5
6j	E	0.493	2.46×10^6	0.00465	0.00320	0.00325	0.0–5.5

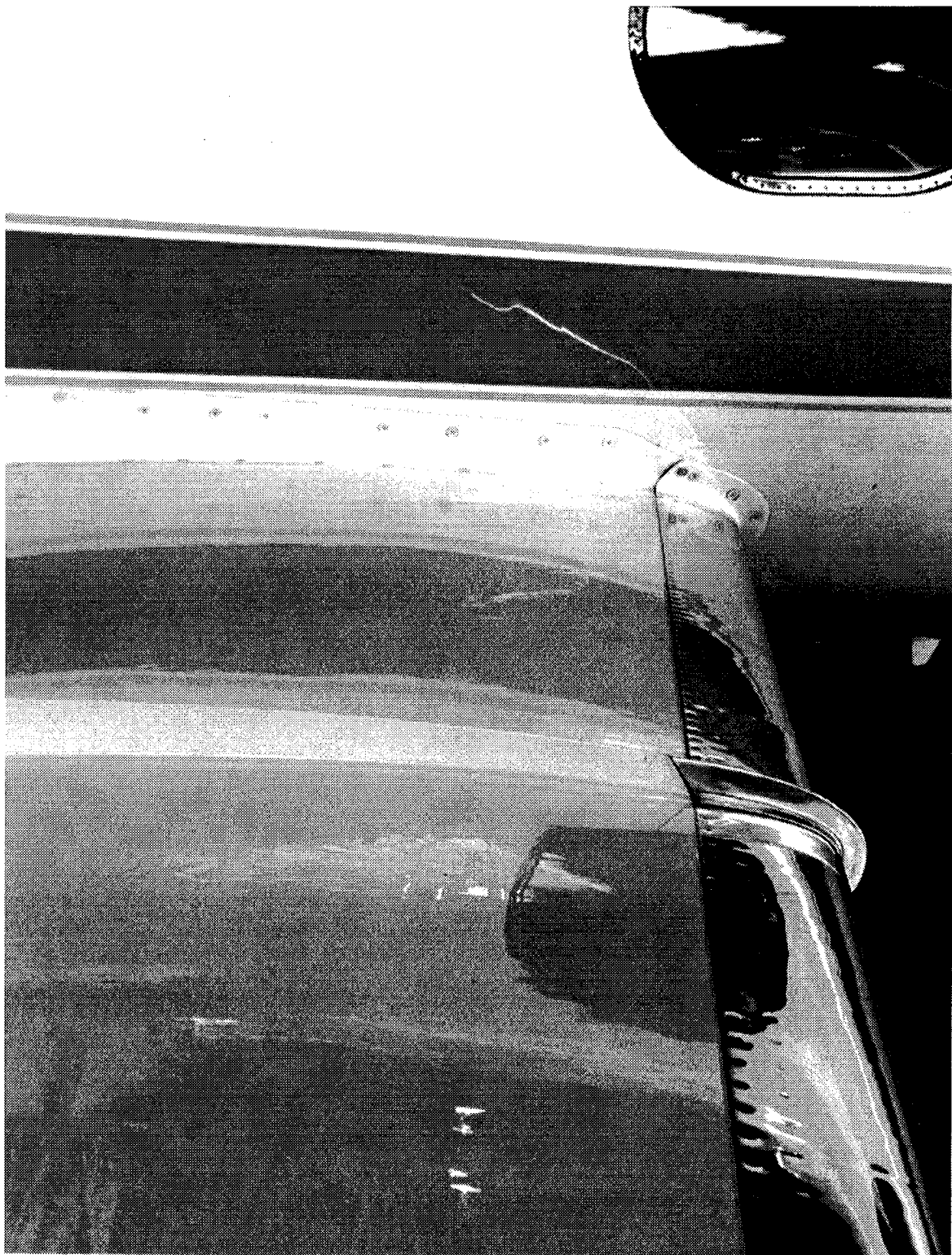


Figure 1. Typical business jet wing leading edge.

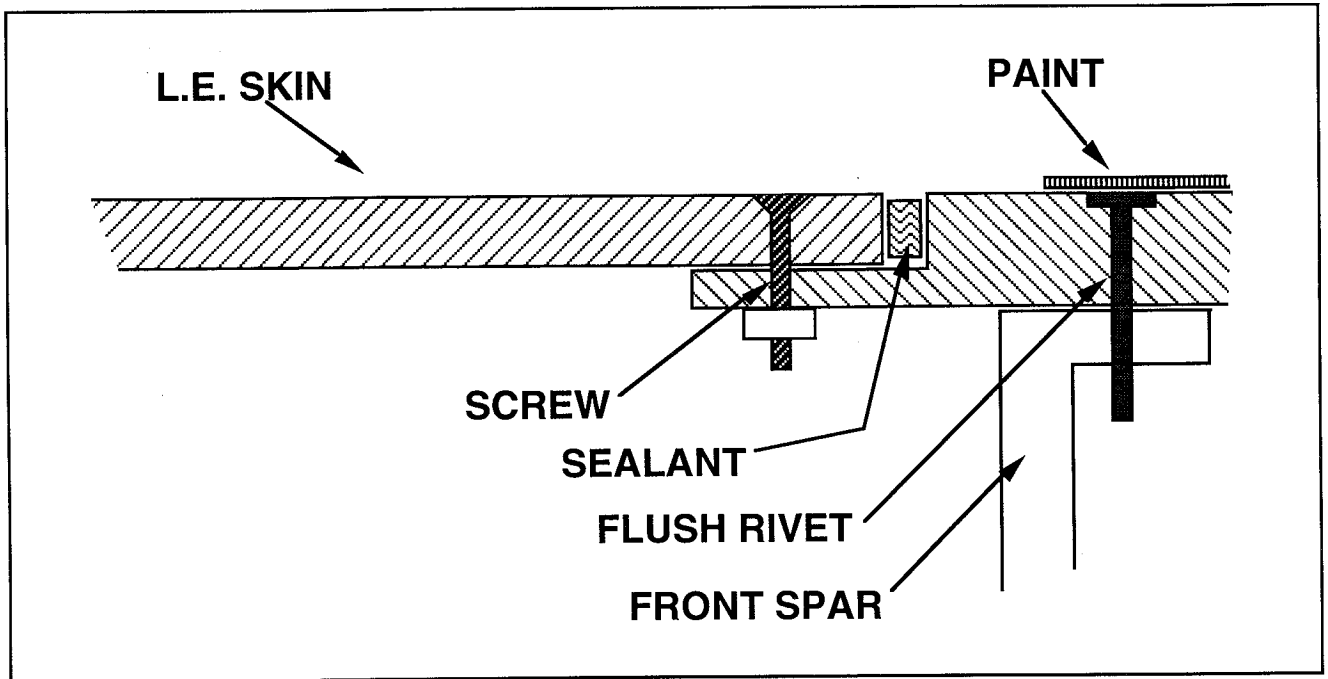


Figure 2(a). Typical business jet wing leading edge assembly.

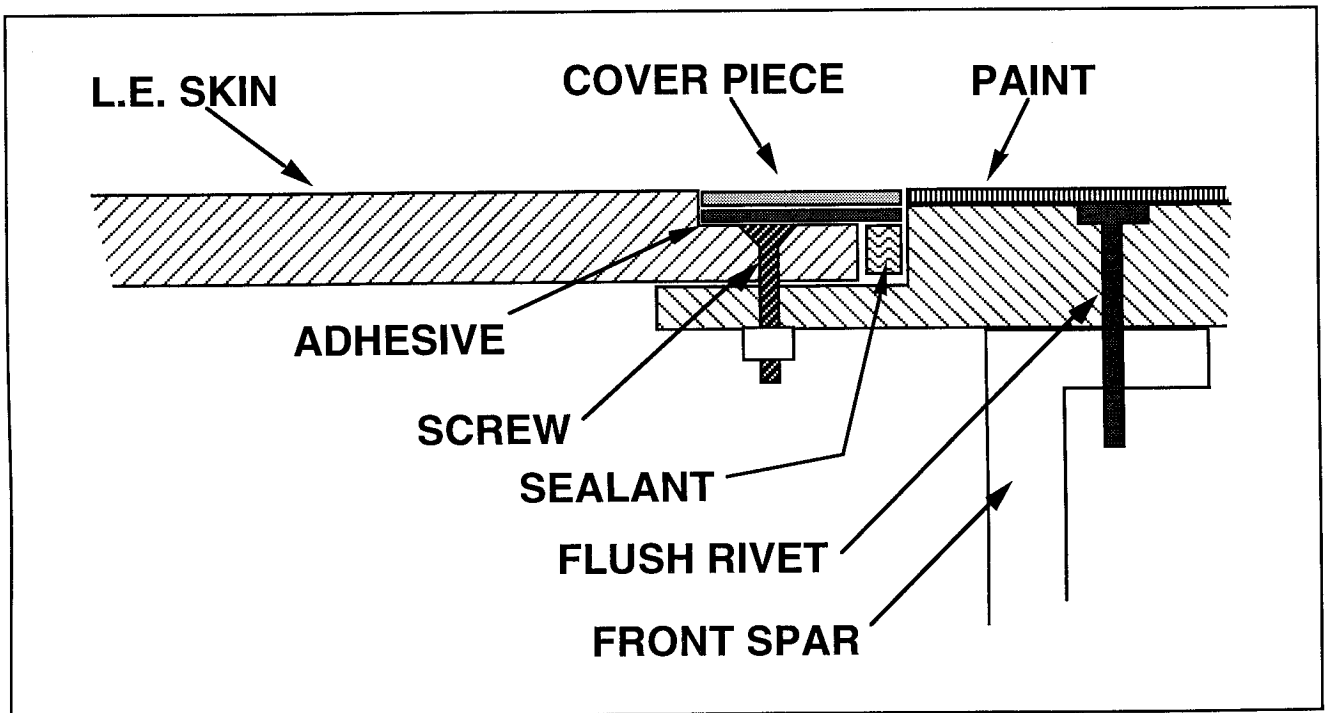


Figure 2(b). Proposed wing leading edge assembly.

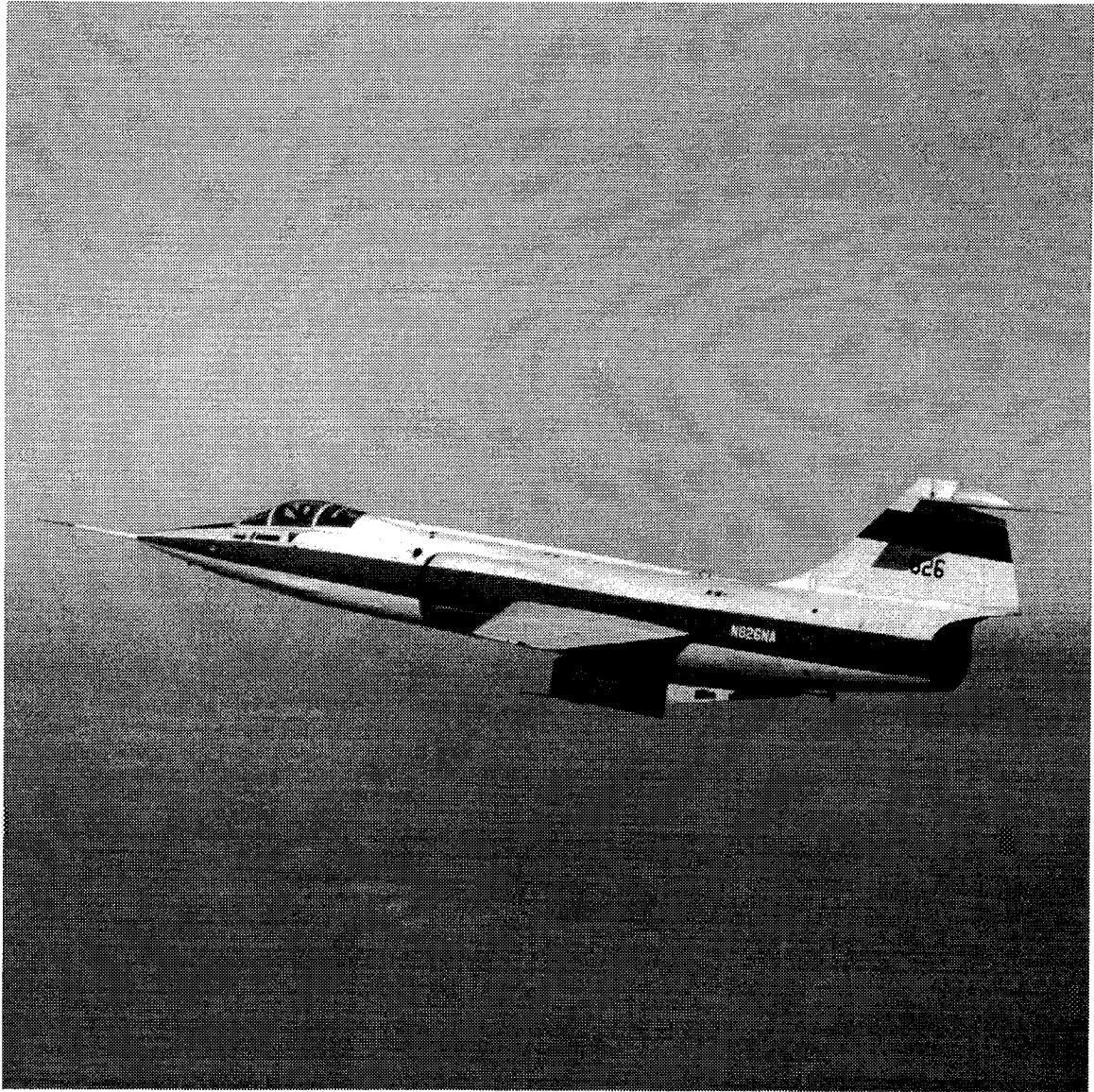


Figure 3. F-104/FTF with Laminar Leading Edge noseshape.

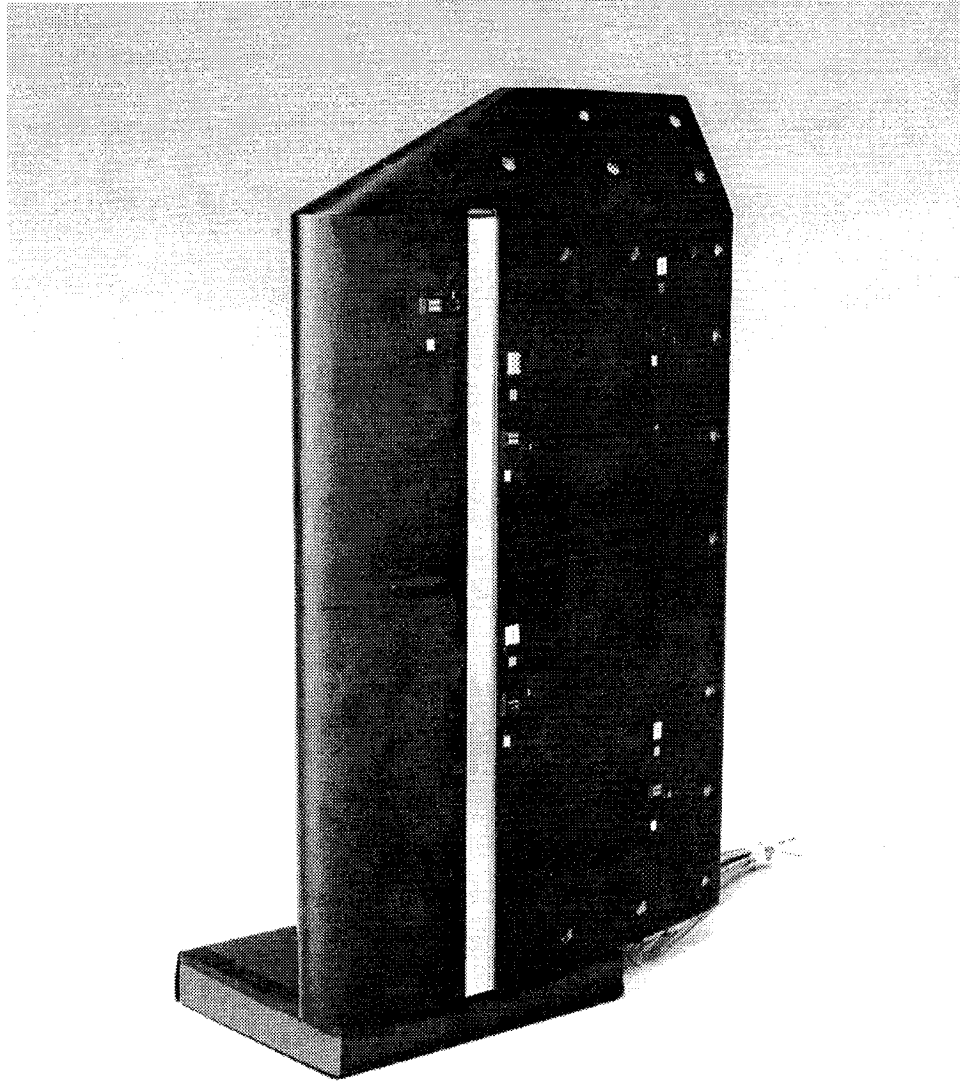


Figure 4. Laminar Leading Edge noseshape.

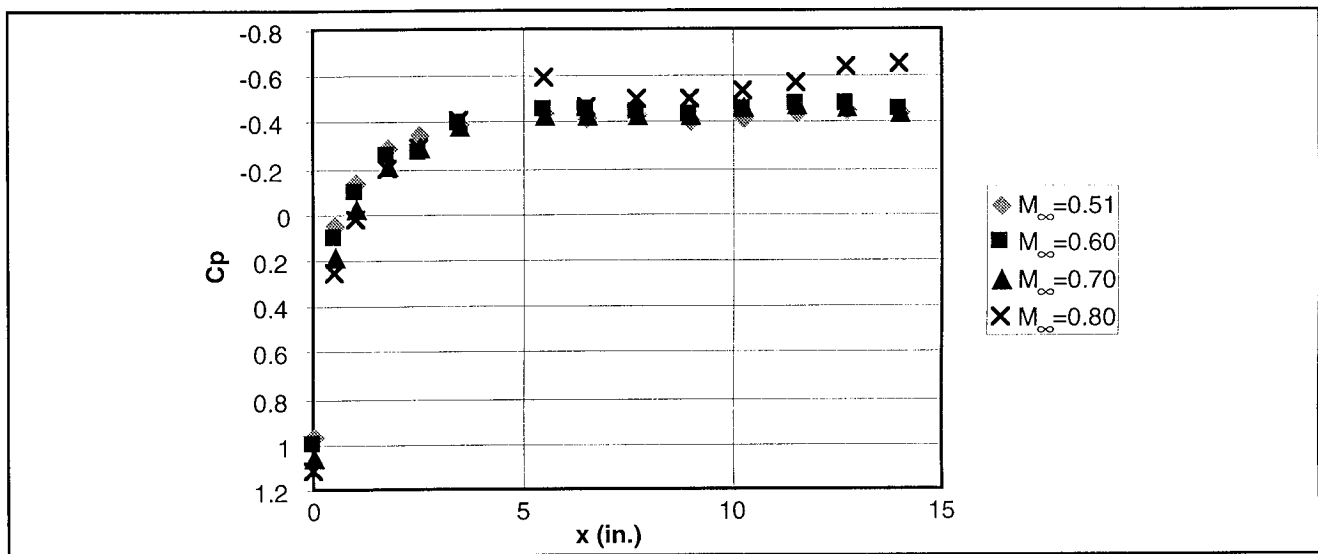


Figure 5(a). Noseshape pressure distributions for $Re = 1.5 \times 10^6$.

x (in)	$M_{\infty}=0.51$	$M_{\infty}=0.60$	$M_{\infty}=0.70$	$M_{\infty}=0.80$
0.00	0.972	1.000	1.057	1.121
0.50	0.051	0.109	0.191	0.255
1.00	-0.141	-0.090	-0.019	0.025
1.75	-0.294	-0.256	-0.203	-0.191
2.50	-0.345	-0.269	-0.292	-0.293
3.50	-0.396	-0.397	-0.381	-0.408
5.50	-0.435	-0.449	-0.432	-0.586
6.50	-0.422	-0.450	-0.433	-0.459
7.75	-0.428	-0.442	-0.433	-0.497
9.00	-0.409	-0.423	-0.432	-0.498
10.25	-0.416	-0.449	-0.457	-0.535
11.50	-0.436	-0.474	-0.470	-0.573
12.75	-0.448	-0.476	-0.464	-0.637
14.00	-0.435	-0.455	-0.445	-0.650

Figure 5(b). Noseshape pressure distributions for $Re = 1.5 \times 10^6$.

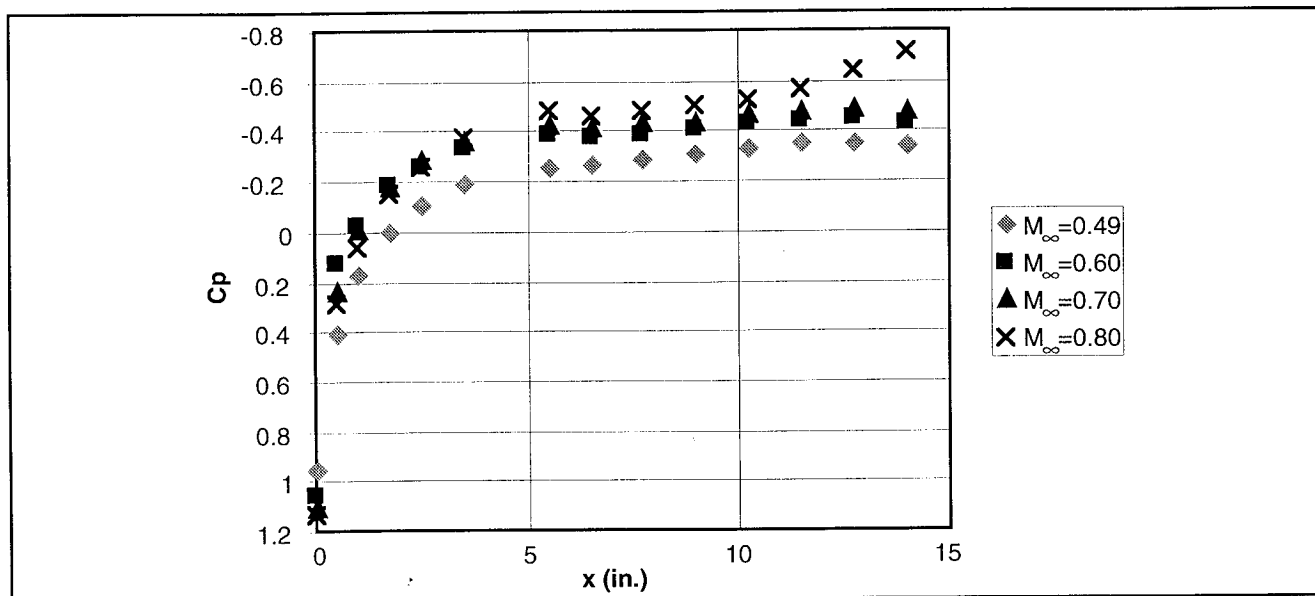


Figure 6(a). Noseshape pressure distributions for $Re = 2.5 \times 10^6$.

x (in)	$M_{\infty}=0.49$	$M_{\infty}=0.60$	$M_{\infty}=0.70$	$M_{\infty}=0.80$
0.00	0.955	1.056	1.105	1.132
0.50	0.411	0.135	0.235	0.289
1.00	0.177	-0.023	-0.012	0.063
1.75	0.000	-0.176	-0.182	-0.145
2.50	-0.101	-0.258	-0.282	-0.252
3.50	-0.190	-0.329	-0.365	-0.377
5.50	-0.253	-0.382	-0.423	-0.484
6.50	-0.266	-0.376	-0.417	-0.453
7.75	-0.291	-0.382	-0.435	-0.484
9.00	-0.304	-0.399	-0.441	-0.497
10.25	-0.329	-0.423	-0.470	-0.522
11.50	-0.348	-0.434	-0.476	-0.566
12.75	-0.354	-0.446	-0.494	-0.641
14.00	-0.342	-0.424	-0.482	-0.717

Figure 6(b). Noseshape pressure distributions for $Re = 2.5 \times 10^6$.

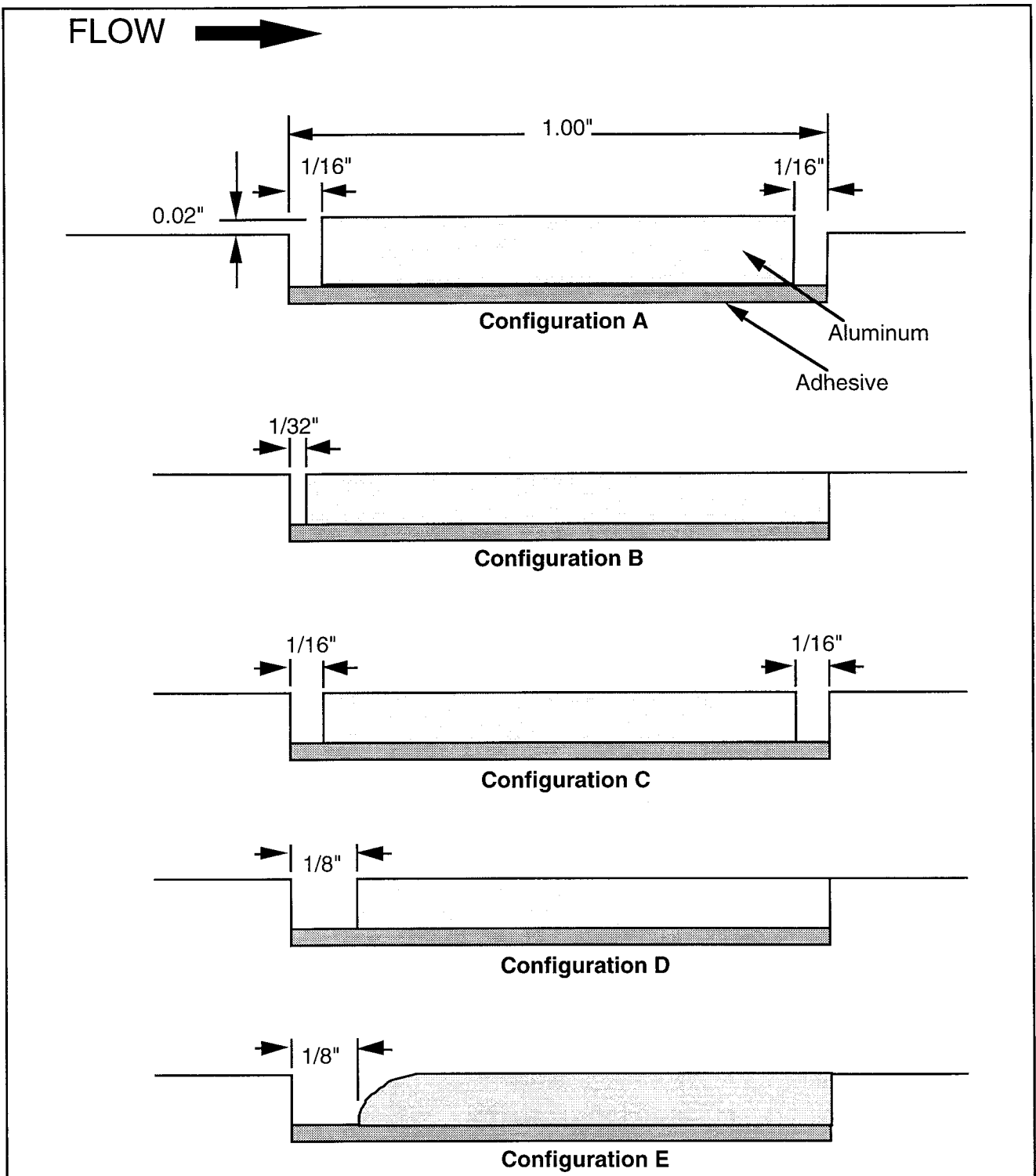
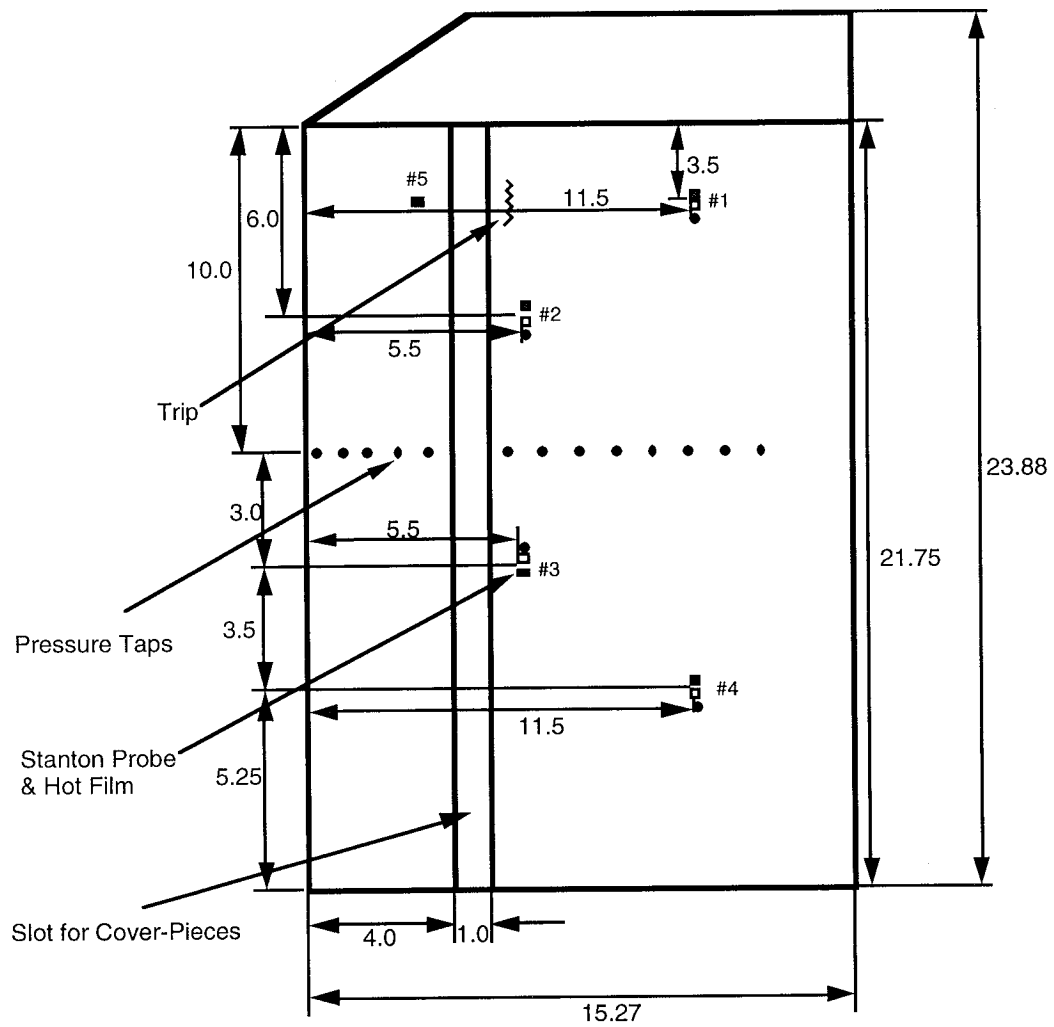


Figure 7. Coverpiece configurations.



- Hot Film gage
- Stanton gage (consists of blade-covered pres. tap and an uncovered adjacent pres. tap)

Pressure taps at specified x locations on both left and right side of nose.
Ten taps on right side, thirteen on left, one on leading edge.

ALL DIMENSIONS IN INCHES

Figure 8. Instrumentation layout.

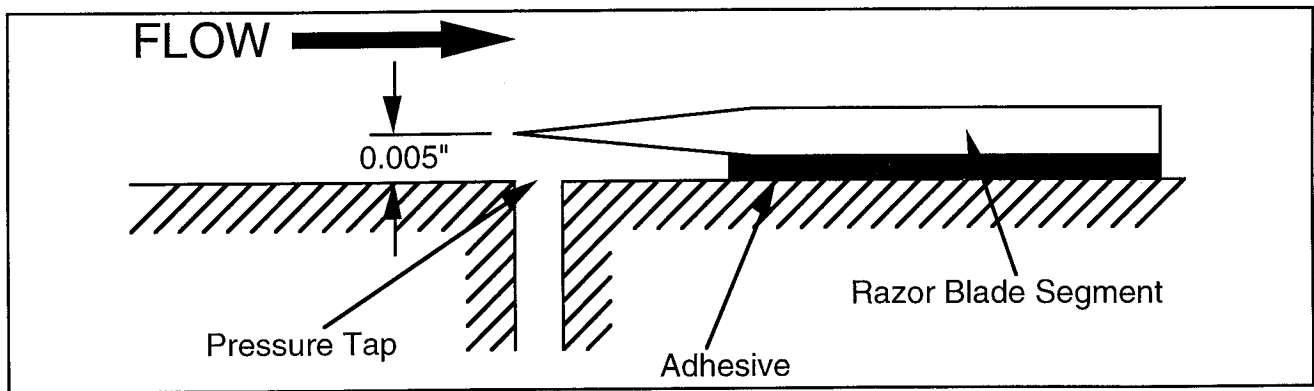


Figure 9(a). Stanton Gauge schematic.

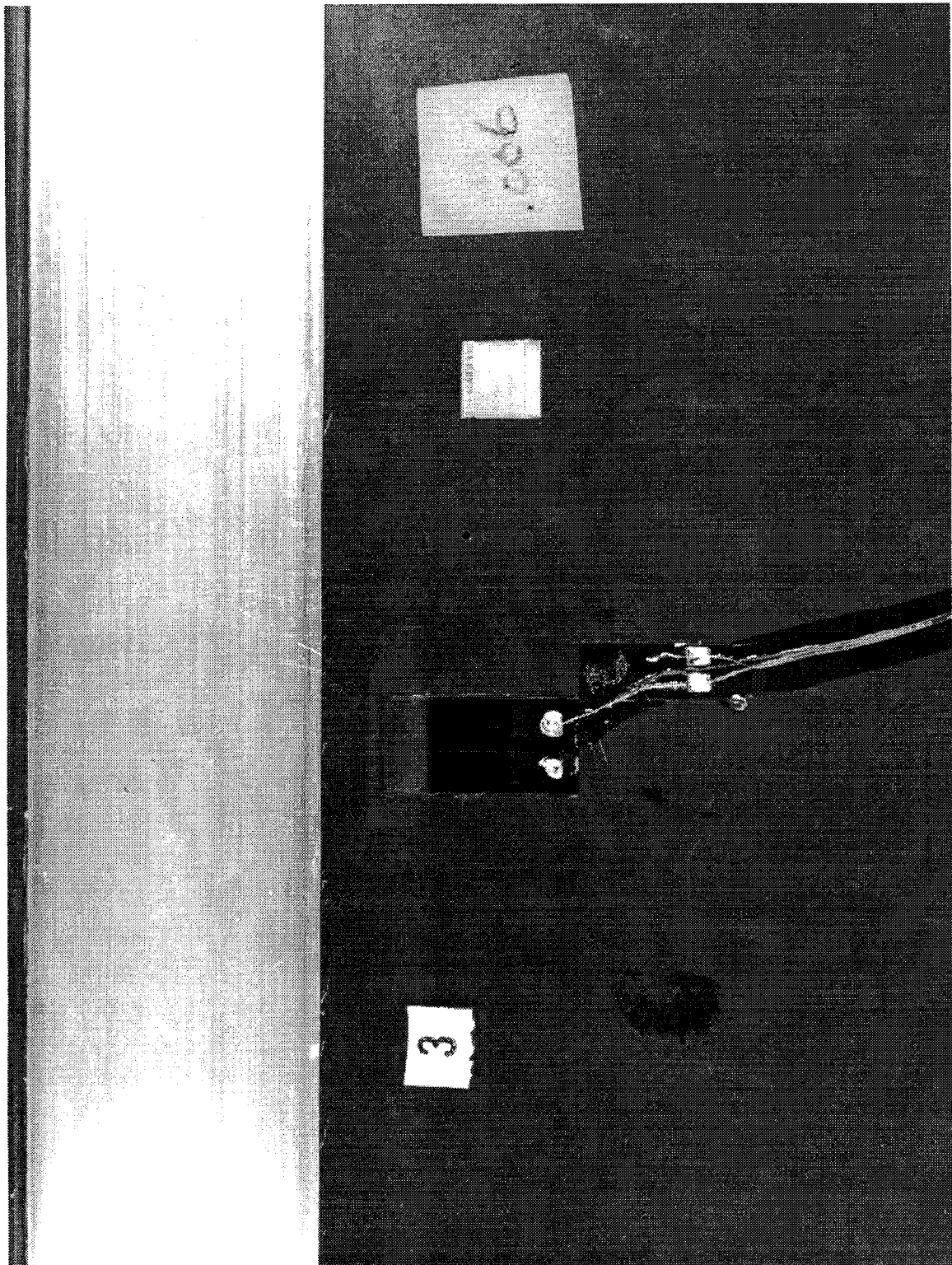


Figure 9(b). Stanton Gauge on Nosepiece.

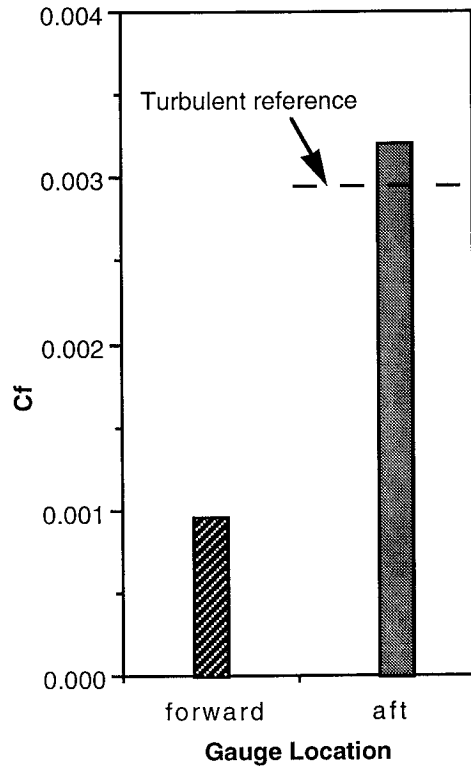


Figure 10(a). Condition 1a, $M_\infty = 0.74$, $Re/ft = 1.57 \times 10^6$.

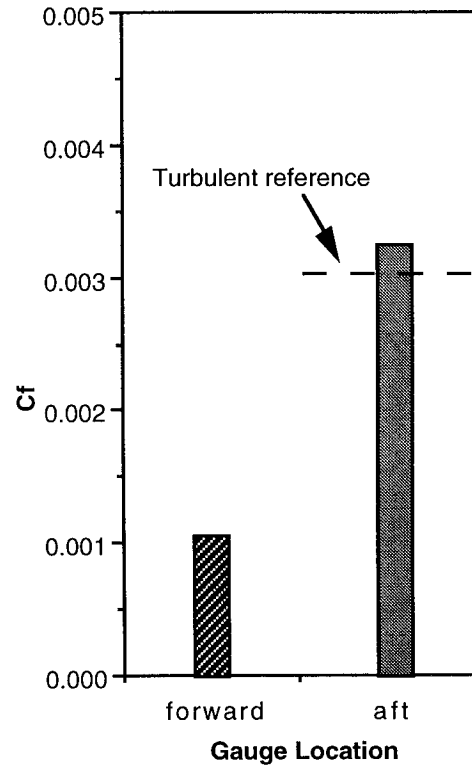


Figure 10(b). Condition 1b, $M_\infty = 0.70$, $Re/ft = 1.53 \times 10^6$.

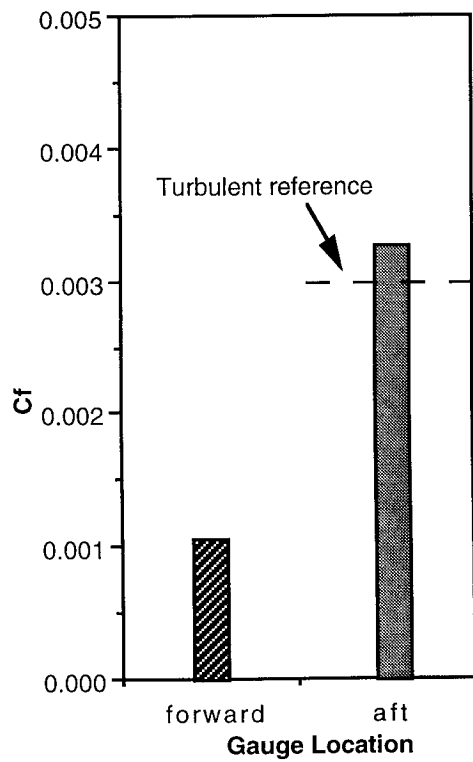


Figure 10(c). Condition 1c, $M_\infty = 0.59$, $Re/ft = 1.45 \times 10^6$.

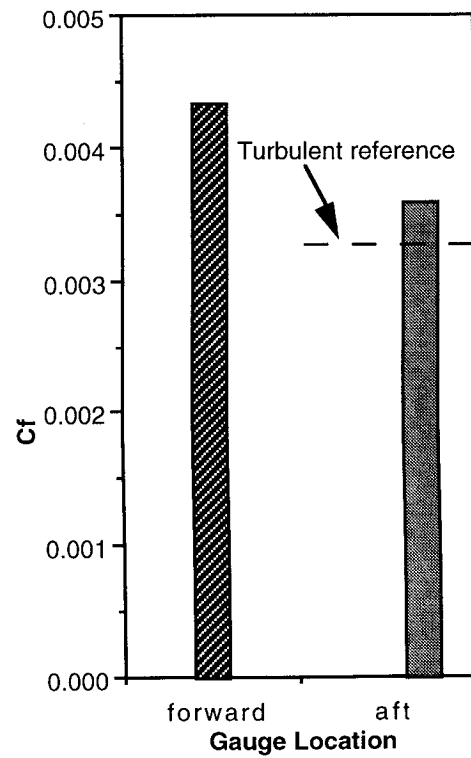


Figure 10(d). Condition 1d, $M_\infty = 0.81$, $Re/ft = 2.44 \times 10^6$.

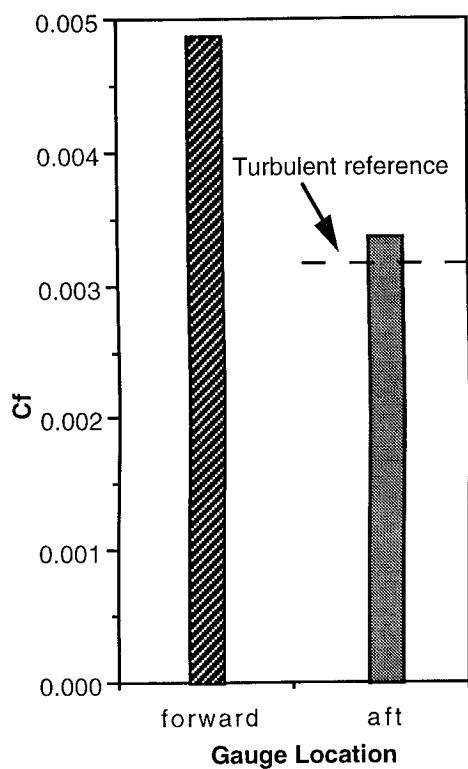


Figure 10(e). Condition 1e, $M_\infty = 0.74$, $Re/ft = 2.40 \times 10^6$.

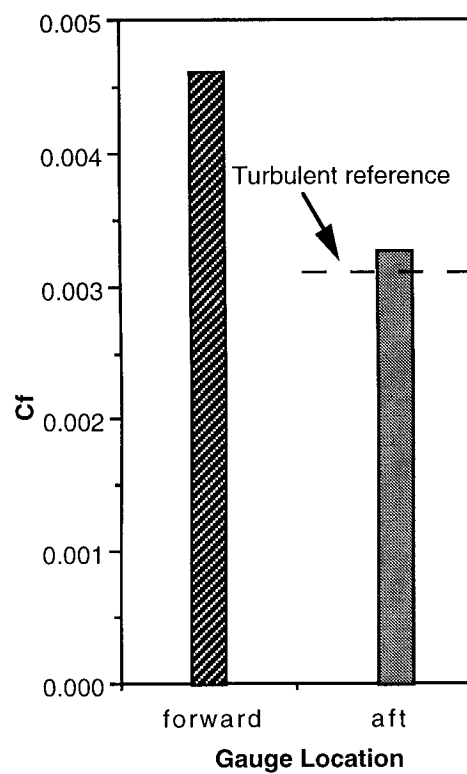


Figure 10(f). Condition 1f, $M_\infty = 0.71$, $Re/ft = 2.42 \times 10^6$.

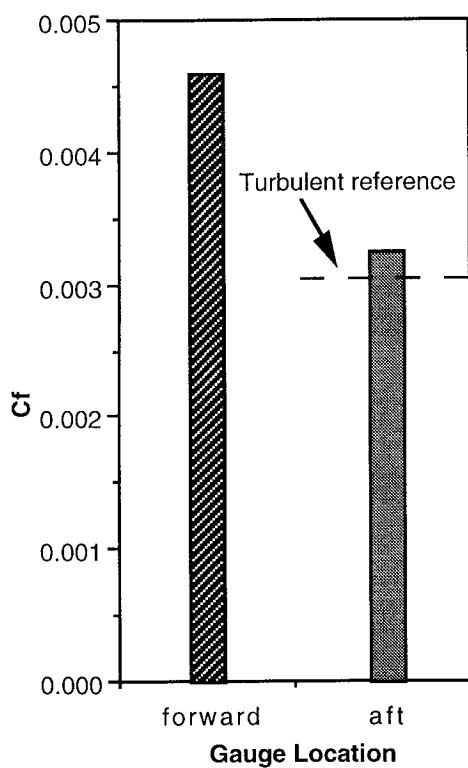


Figure 10(g). Condition 1g, $M_\infty = 0.58$, $Re/ft = 2.33 \times 10^6$.

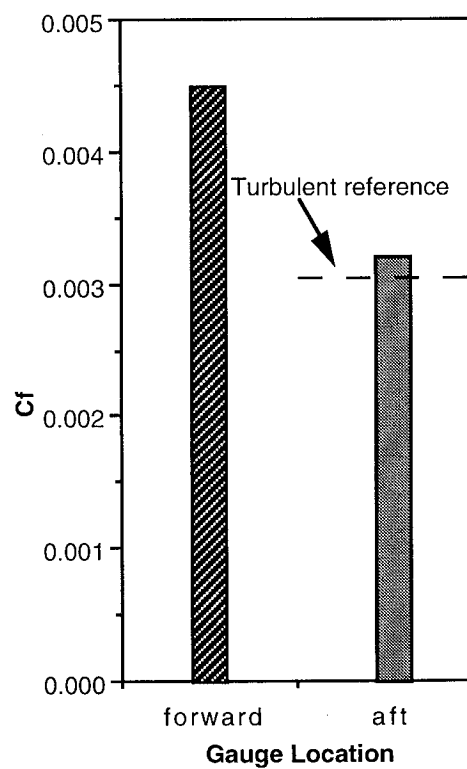


Figure 10(h) Condition 1h, $M_\infty = 0.49$, $Re/ft = 2.34 \times 10^6$.

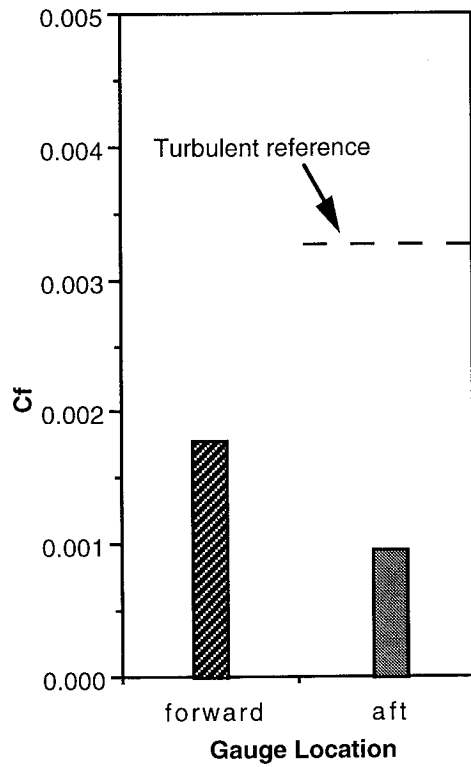


Figure 11(a). Condition 2a, $M_\infty = 0.78$, $Re/ft = 1.47 \times 10^6$.

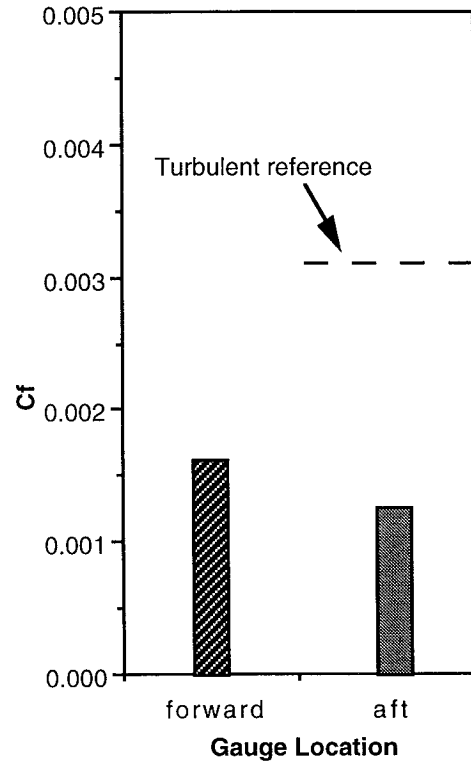


Figure 11(b). Condition 2b, $M_\infty = 0.75$, $Re/ft = 1.55 \times 10^6$.

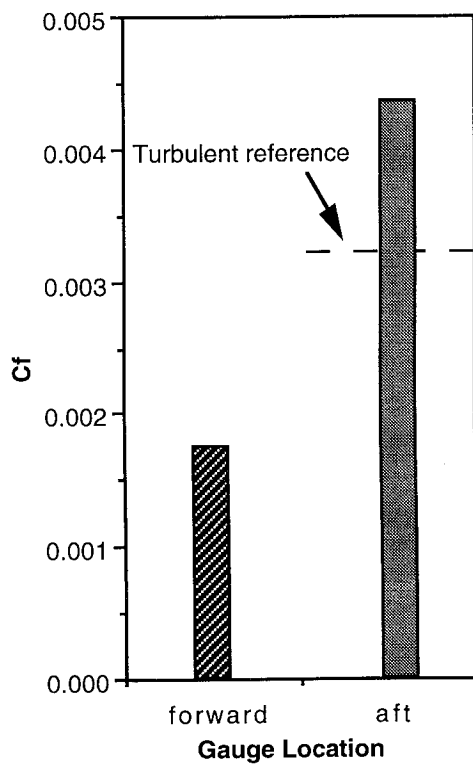


Figure 11(c). Condition 2c, $M_\infty = 0.80$, $Re/ft = 2.03 \times 10^6$.

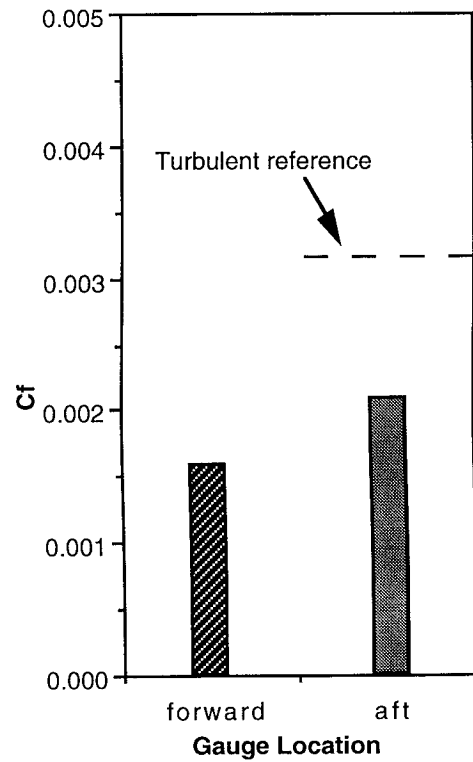


Figure 11(d). Condition 2d, $M_\infty = 0.75$, $Re/ft = 1.99 \times 10^6$.

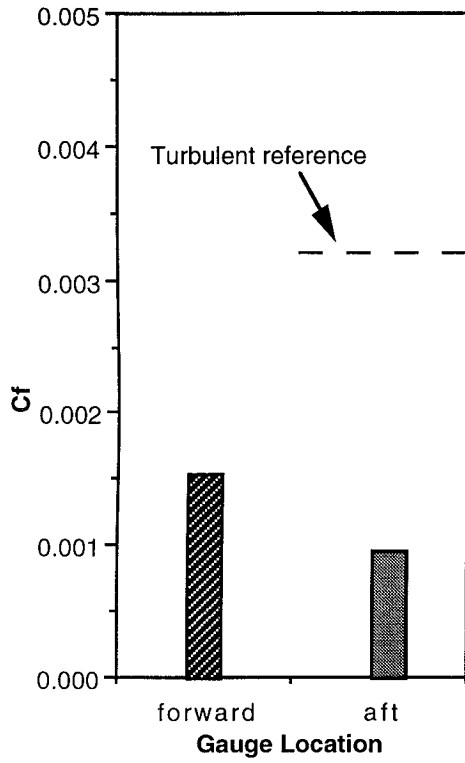


Figure 11(e). Condition 2e, $M_\infty = 0.60$, $Re/ft = 1.52 \times 10^6$.

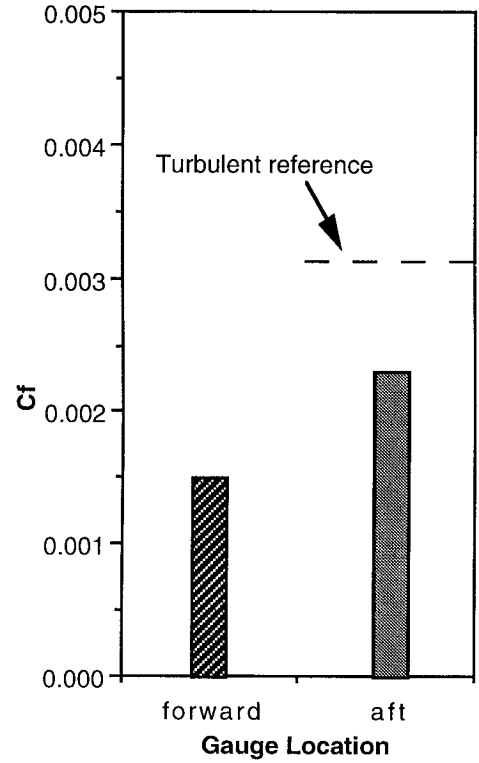


Figure 11(f). Condition 2f, $M_\infty = 0.70$, $Re/ft = 1.99 \times 10^6$.

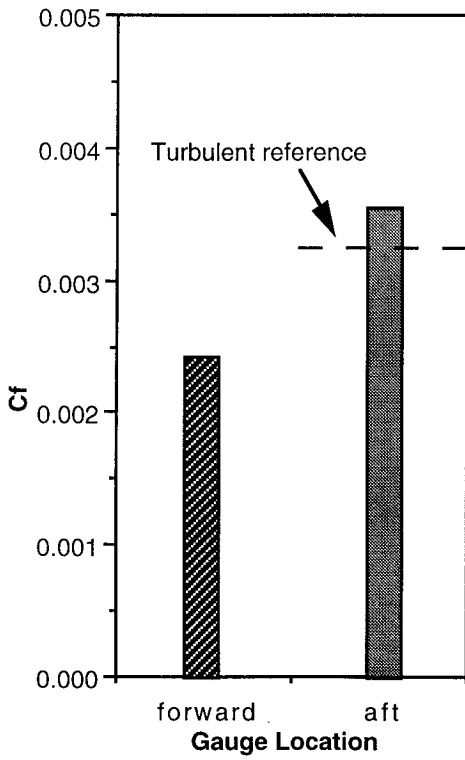


Figure 11(g). Condition 2g, $M_\infty = 0.80$, $Re/ft = 2.50 \times 10^6$.

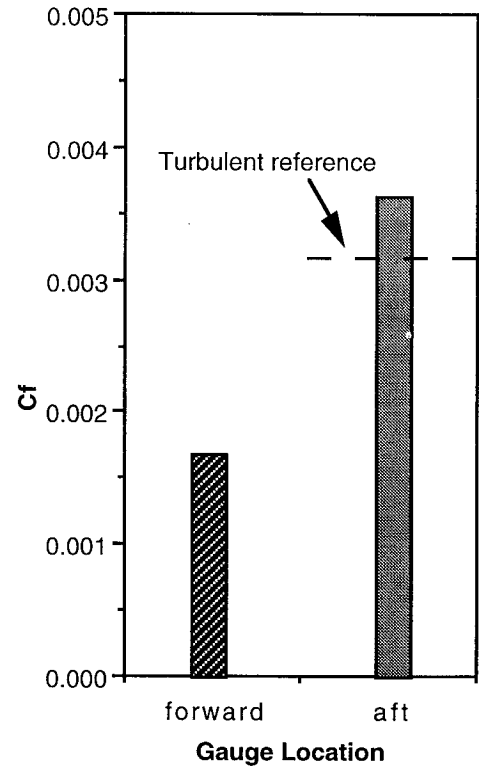


Figure 11(h). Condition 2h, $M_\infty = 0.75$, $Re/ft = 2.52 \times 10^6$.

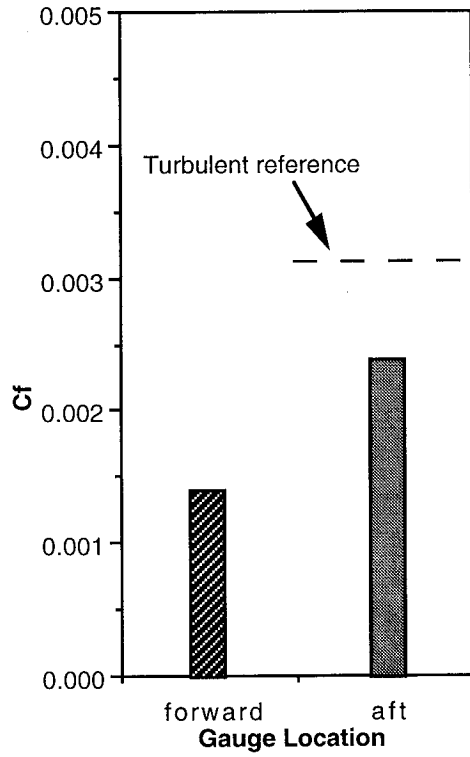


Figure 11(i). Condition 2i, $M_\infty = 0.60$, $Re/ft = 1.98 \times 10^6$.

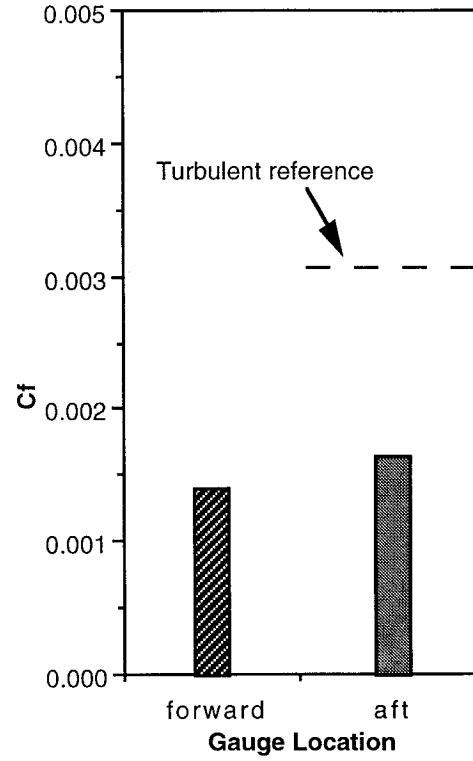


Figure 12(a). Condition 3a, $M_\infty = 0.60$, $Re/ft = 1.52 \times 10^6$.

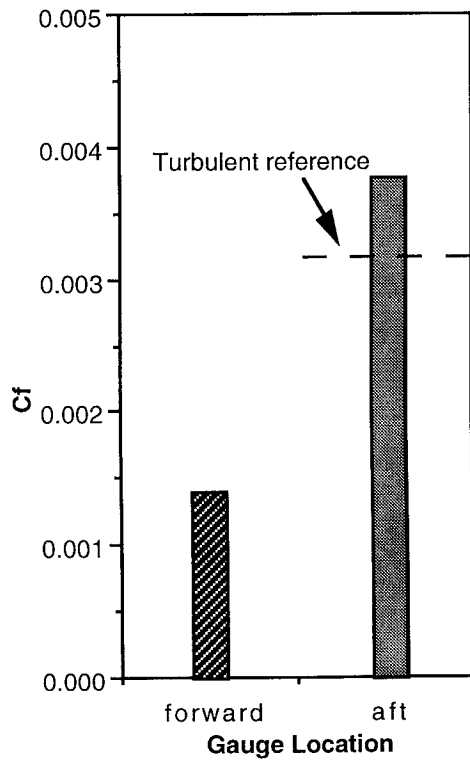


Figure 12(b). Condition 3b, $M_\infty = 0.70$, $Re/ft = 2.51 \times 10^6$.

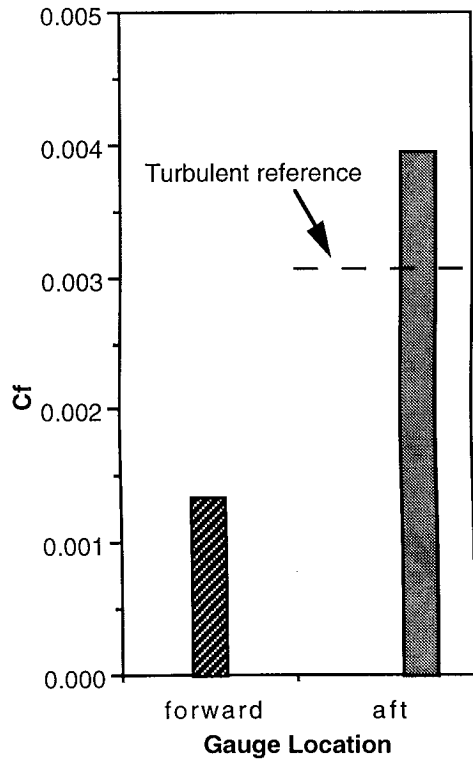


Figure 12(c). Condition 3c, $M_\infty = 0.60$, $Re/ft = 2.52 \times 10^6$.

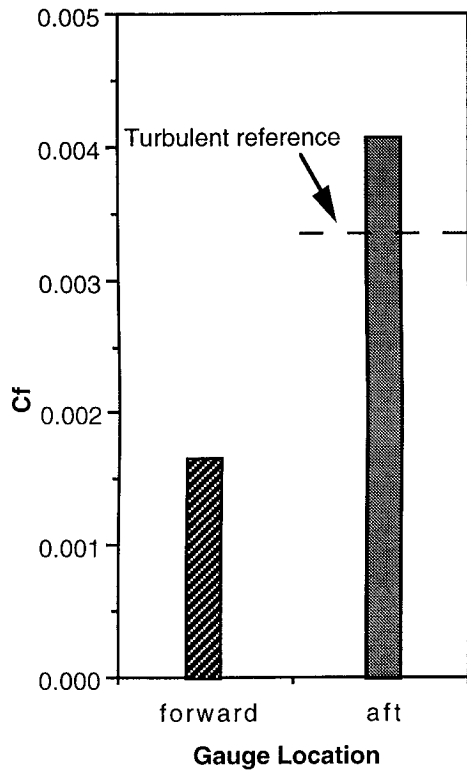


Figure 13(a). Condition 4a, $M_\infty = 0.80$, $Re/ft = 1.57 \times 10^6$.

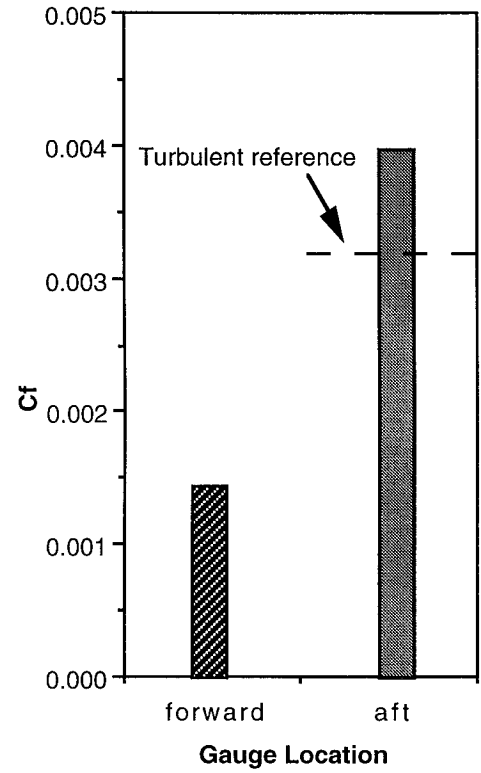


Figure 13(b). Condition 4b, $M_\infty = 0.70$, $Re/ft = 1.51 \times 10^6$.

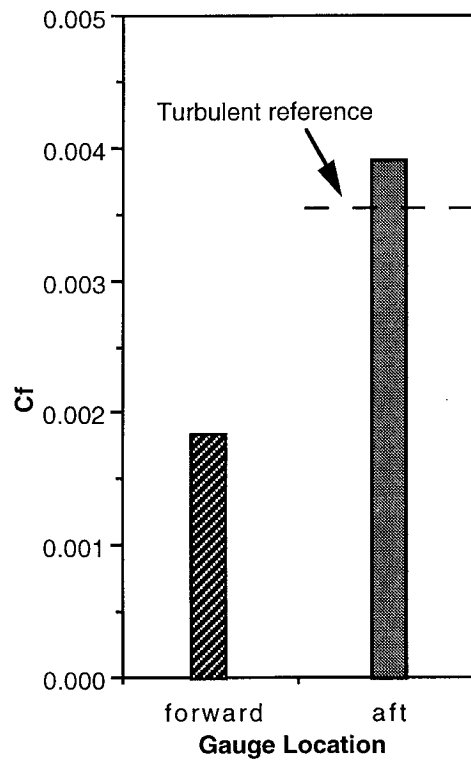


Figure 13(c). Condition 4c, $M_\infty = 0.80$, $Re/ft = 2.03 \times 10^6$.

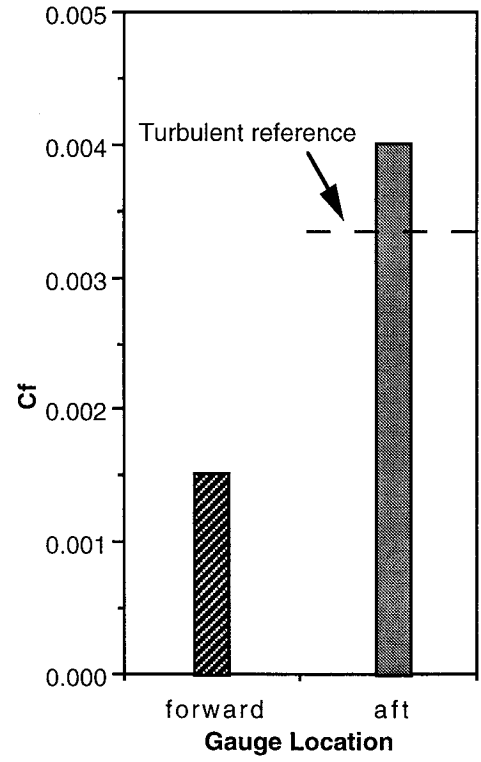


Figure 13(d). Condition 4d, $M_\infty = 0.70$, $Re/ft = 2.00 \times 10^6$.

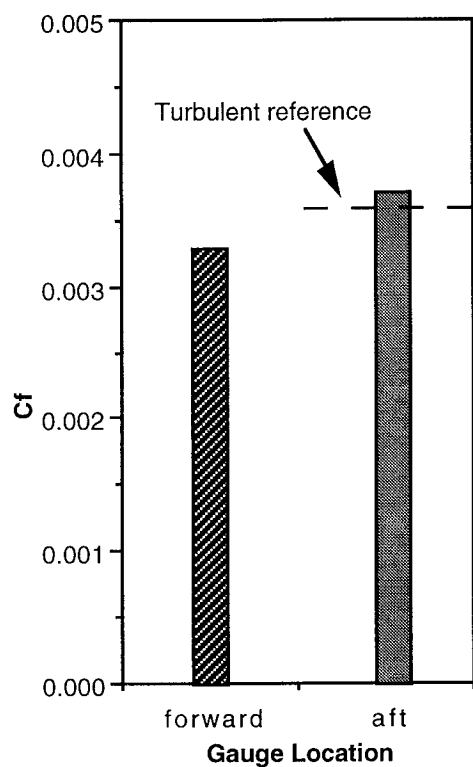


Figure 13(e). Condition 4e, $M_\infty = 0.80$, $Re/ft = 2.44 \times 10^6$.

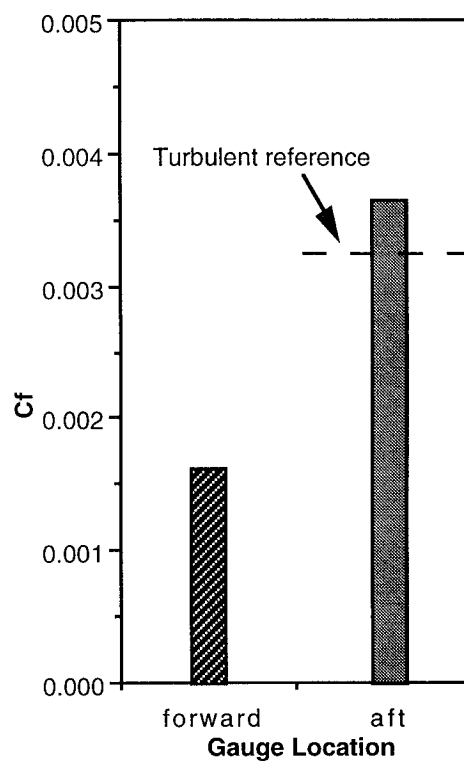


Figure 13(f). Condition 4f, $M_\infty = 0.70$, $Re/ft = 2.52 \times 10^6$.

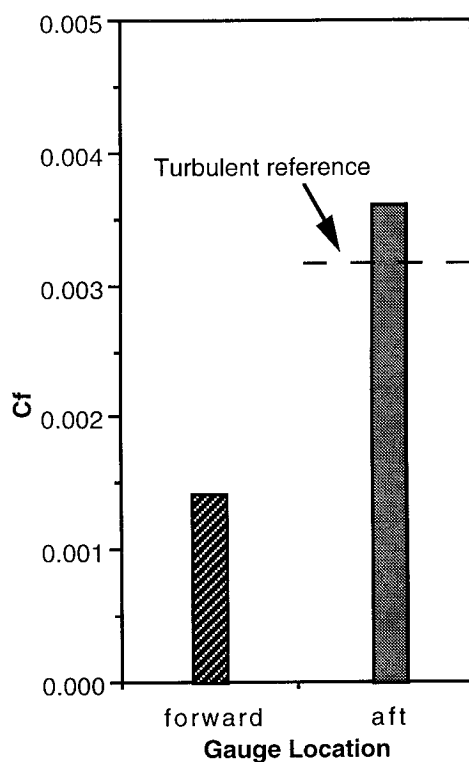


Figure 13(g). Condition 4g, $M_\infty = 0.60$, $Re/ft = 2.52 \times 10^6$.

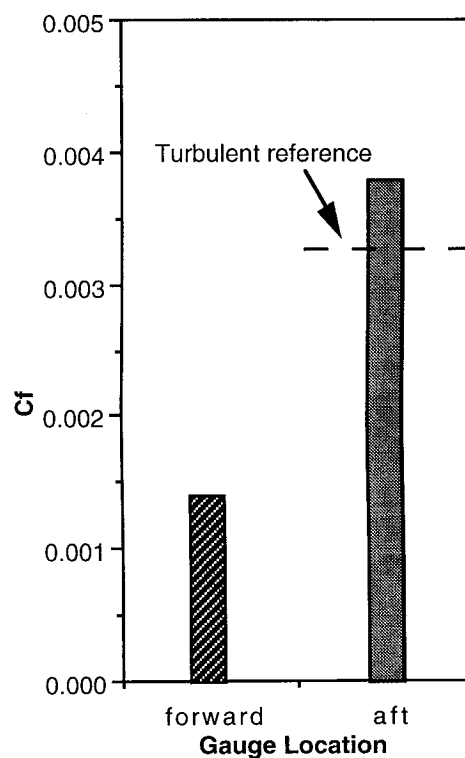


Figure 13(h). Condition 4h, $M_\infty = 0.61$, $Re/ft = 2.02 \times 10^6$.

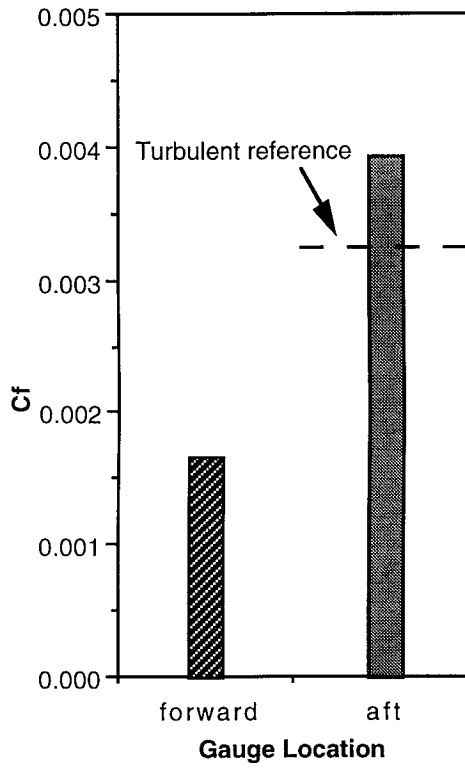


Figure 13(i). Condition 4i, $M_\infty = 0.51$, $Re/ft = 2.03 \times 10^6$.

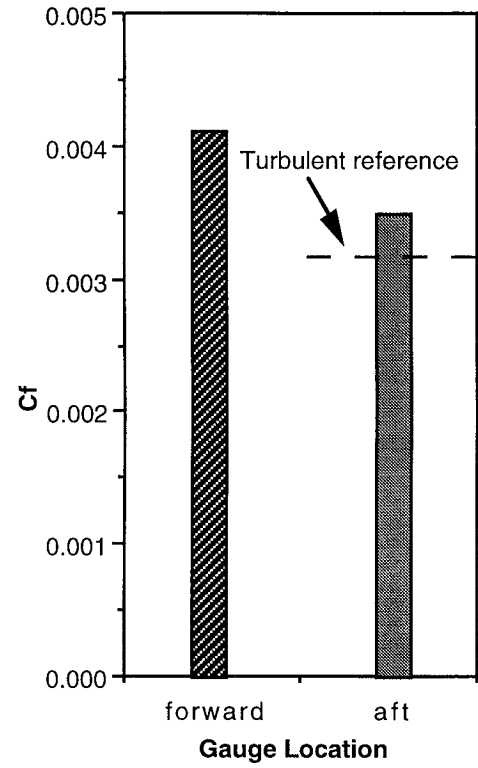


Figure 13(j). Condition 4j, $M_\infty = 0.50$, $Re/ft = 2.47 \times 10^6$.

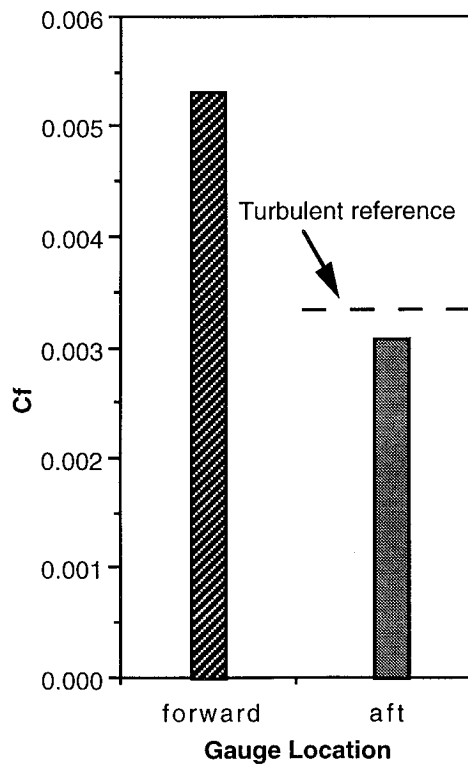


Figure 14(a). Condition 5a, $M_\infty = 0.80$, $Re/ft = 1.54 \times 10^6$.

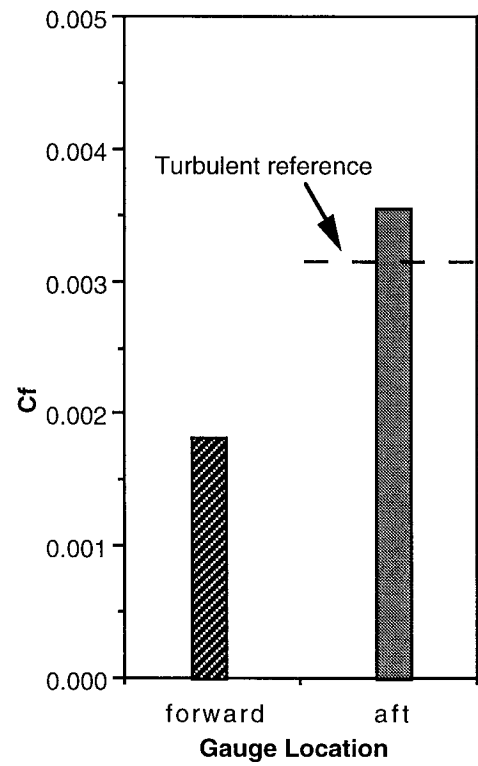


Figure 14(b). Condition 5b, $M_\infty = 0.69$, $Re/ft = 1.46 \times 10^6$.

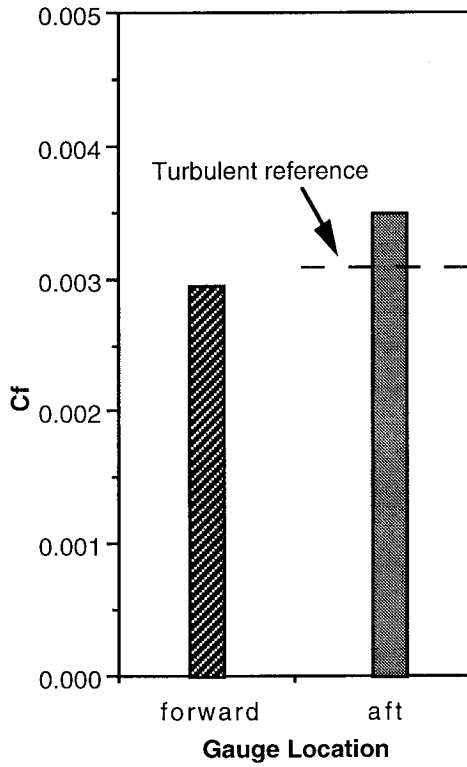


Figure 14(c). Condition 5c, $M_\infty = 0.60$, $Re/ft = 1.51 \times 10^6$.

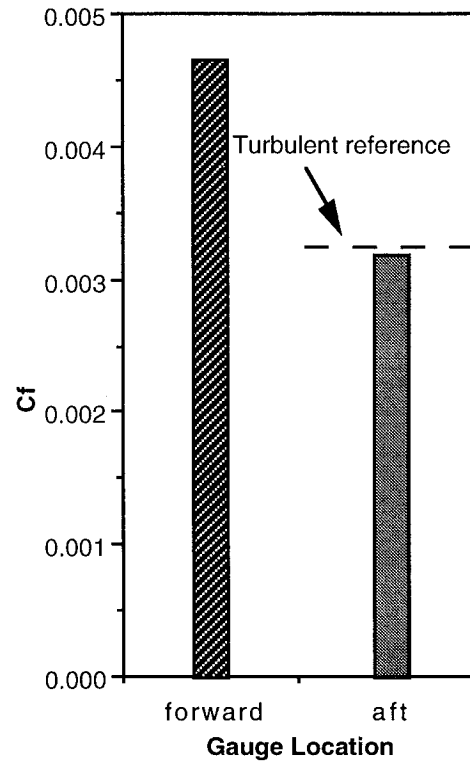


Figure 14(d). Condition 5d, $M_\infty = 0.70$, $Re/ft = 2.00 \times 10^6$.

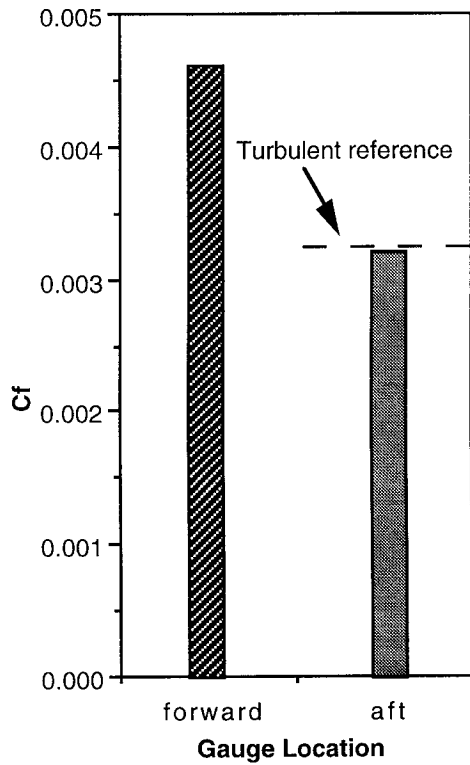


Figure 14(e). Condition 5e, $M_\infty = 0.69$, $Re/ft = 2.48 \times 10^6$.

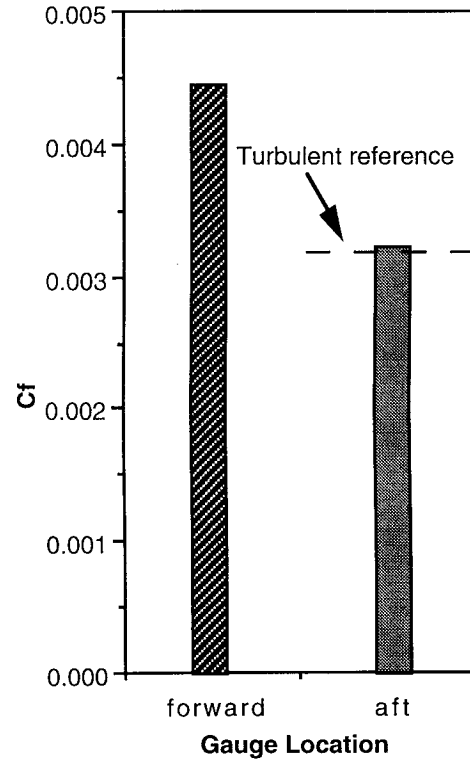


Figure 14(f). Condition 5f, $M_\infty = 0.60$, $Re/ft = 2.51 \times 10^6$.

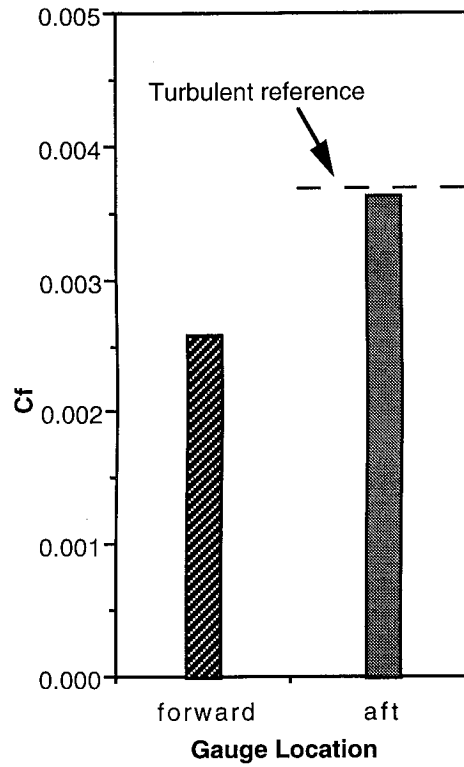


Figure 15(a). Condition 6a, $M_\infty = 0.80$, $Re/ft = 1.49 \times 10^6$.

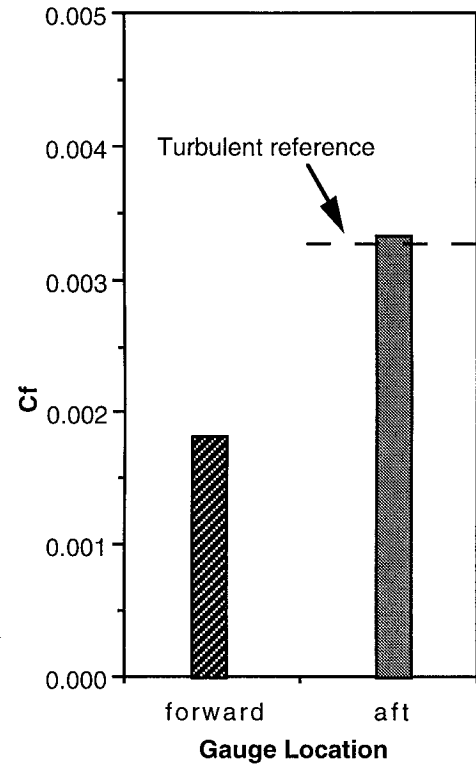


Figure 15(b). Condition 6b, $M_\infty = 0.71$, $Re/ft = 1.53 \times 10^6$.

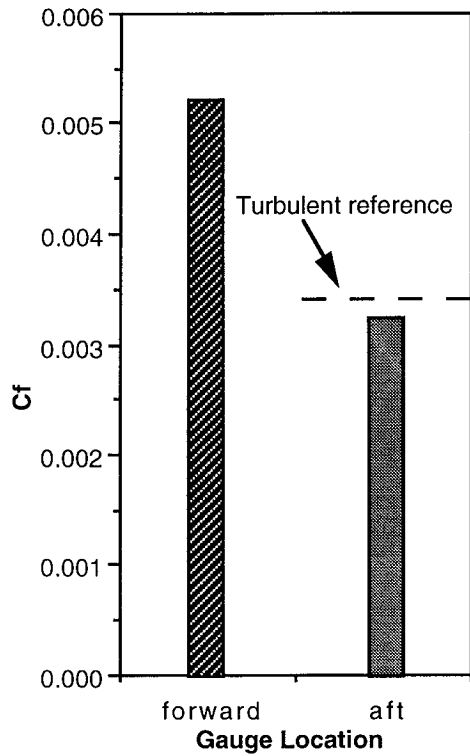


Figure 15(c). Condition 6c, $M_\infty = 0.81$, $Re/ft = 2.08 \times 10^6$.

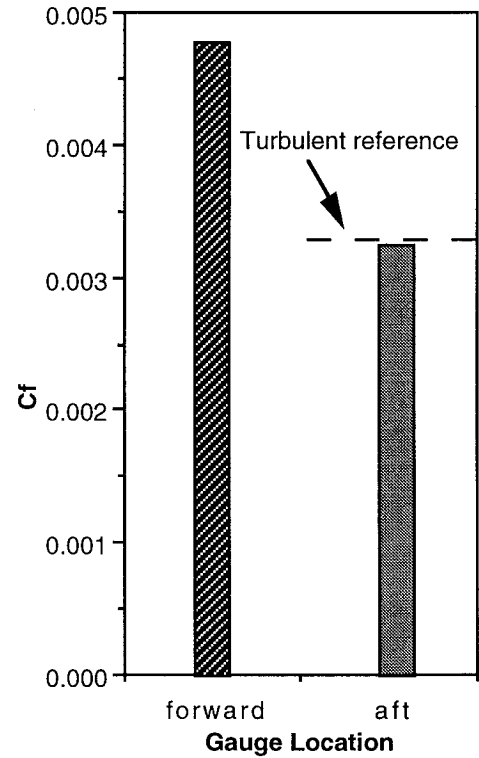


Figure 15(d). Condition 6d, $M_\infty = 0.73$, $Re/ft = 2.08 \times 10^6$.

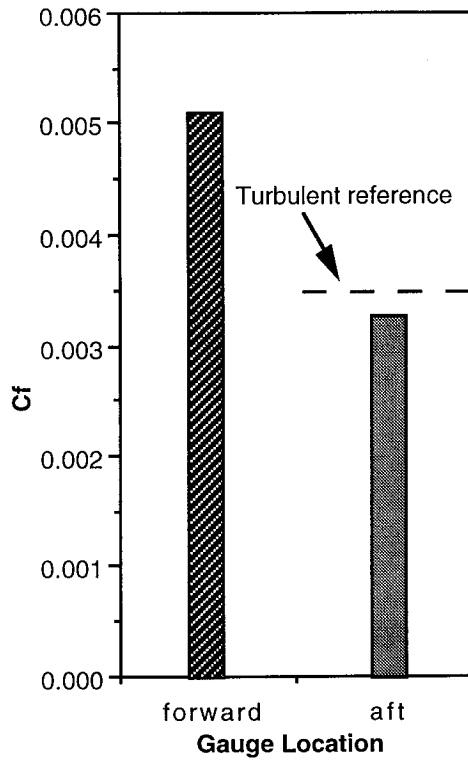


Figure 15(e). Condition 6e, $M_\infty = 0.80$, $Re/ft = 2.51 \times 10^6$.

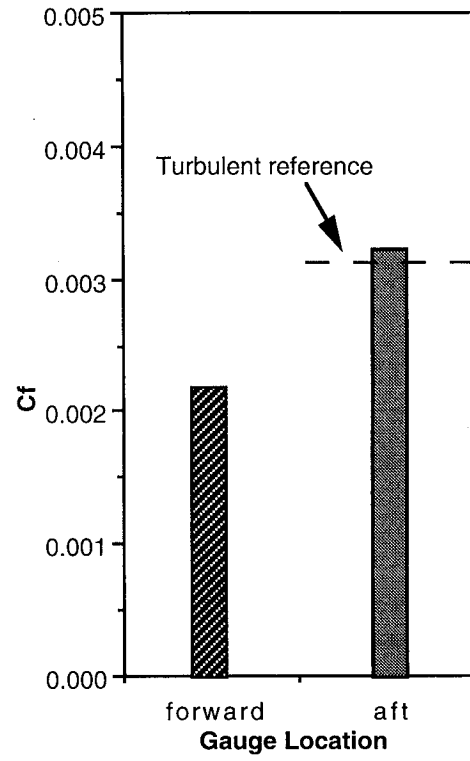


Figure 15(f). Condition 6f, $M_\infty = 0.51$, $Re/ft = 1.54 \times 10^6$.

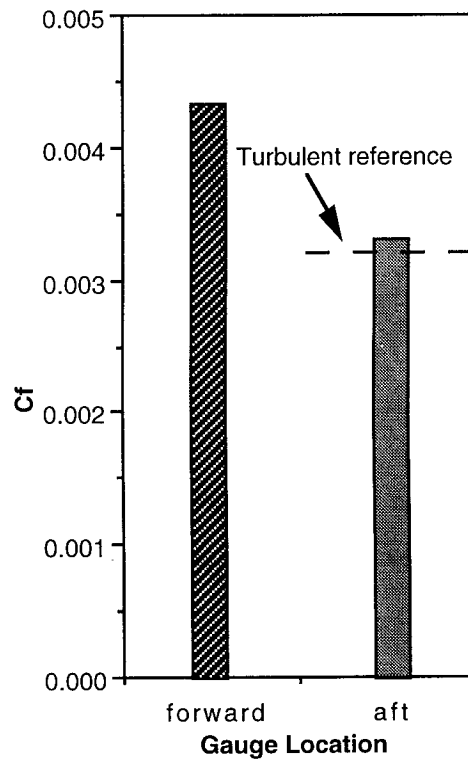


Figure 15(g). Condition 6g, $M_\infty = 0.60$, $Re/ft = 1.97 \times 10^6$.

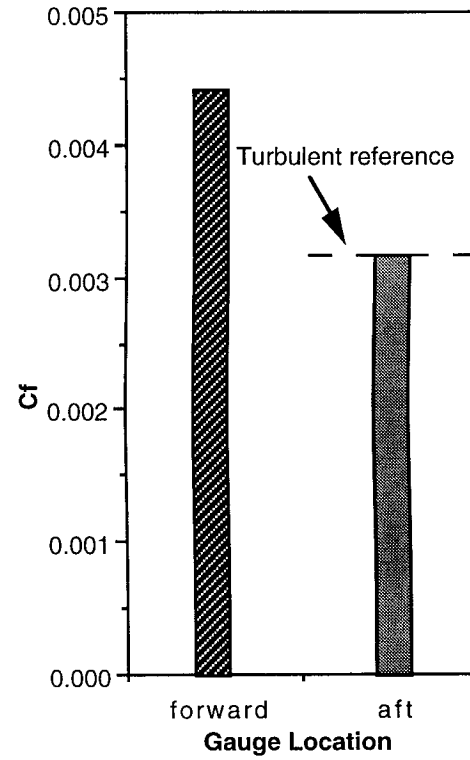


Figure 15(h). Condition 6h, $M_\infty = 0.60$, $Re/ft = 2.54 \times 10^6$.

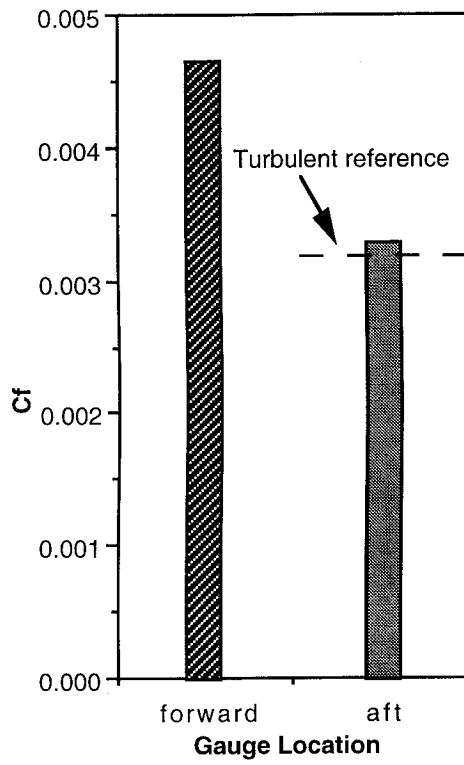


Figure 15(i). Condition 6i, $M_\infty = 0.50$, $Re/ft = 2.02 \times 10^6$.

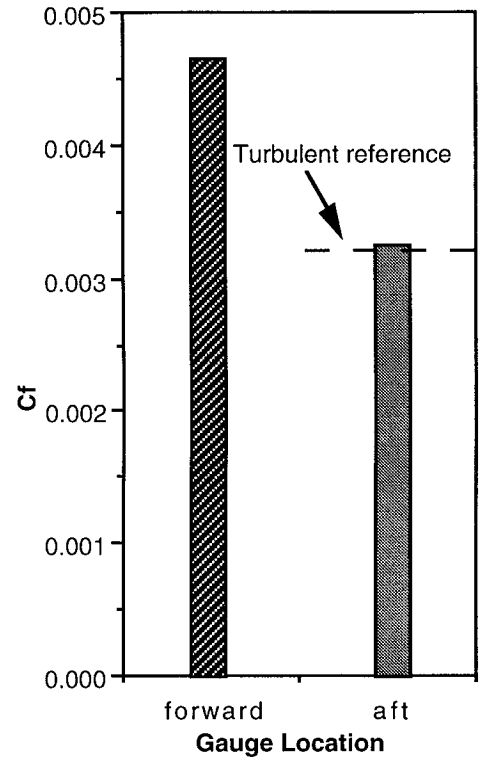


Figure 15(j). Condition 6j, $M_\infty = 0.49$, $Re/ft = 2.46 \times 10^6$.

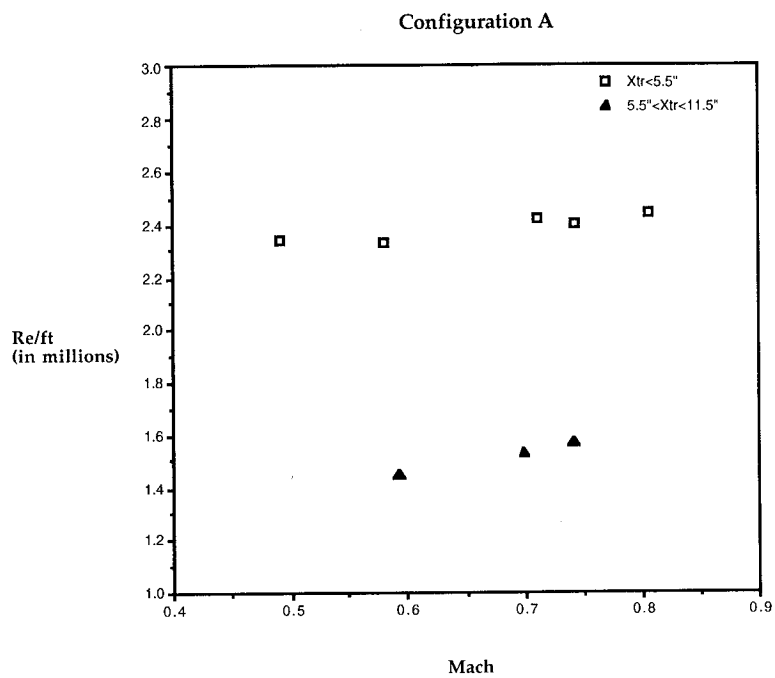


Figure 16. Summary of results for Cover-Piece Configuration A.

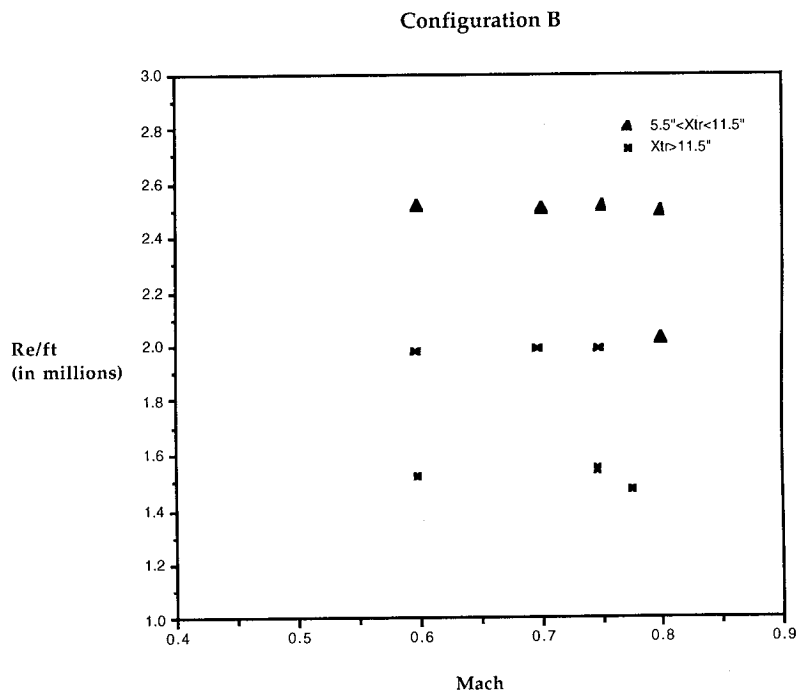


Figure 17. Summary of results for Cover-Piece Configuration B.

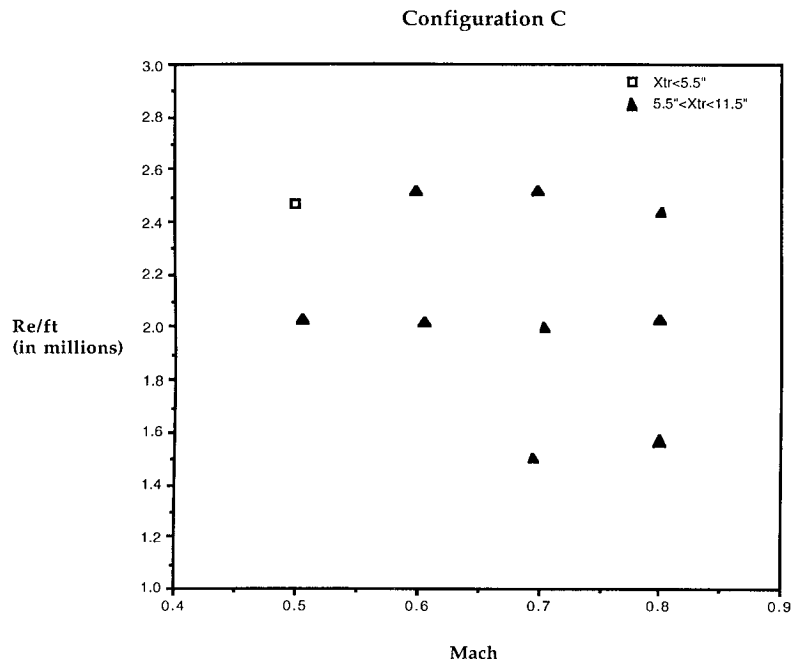


Figure 18. Summary of results for Cover-Piece Configuration C.

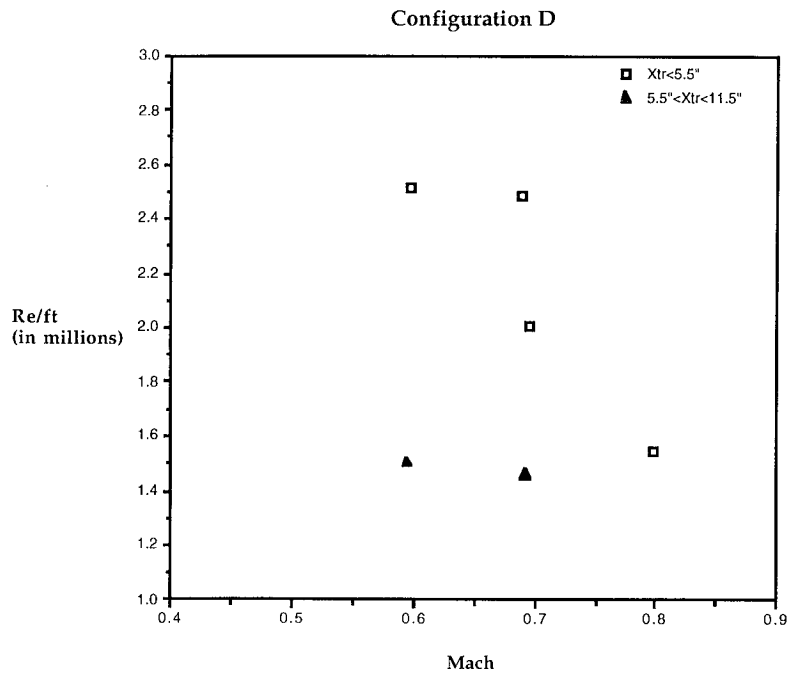


Figure 19. Summary of results for Cover-Piece Configuration D.

REPORT DOCUMENTATION PAGE			Form Approved OMB No. 0704-0188	
Public reporting burden for this collection of information is estimated to average 1 hour per response, including the time for reviewing instructions, searching existing data sources, gathering and maintaining the data needed, and completing and reviewing the collection of information. Send comments regarding this burden estimate or any other aspect of this collection of information, including suggestions for reducing this burden, to Washington Headquarters Services, Directorate for Information Operations and Reports, 1215 Jefferson Davis Highway, Suite 1204, Arlington, VA 22202-4302, and to the Office of Management and Budget, Paperwork Reduction Project (0704-0188), Washington, DC 20503.				
1. AGENCY USE ONLY (Leave blank)		2. REPORT DATE October 1996		3. REPORT TYPE AND DATES COVERED Technical Memorandum
4. TITLE AND SUBTITLE Wing Leading Edge Joint Laminar Flow Tests			5. FUNDING NUMBERS 505-59-20	
6. AUTHOR(S) Aaron Drake, Russell V. Westphal, Fanny A. Zuniga, Robert A. Kennelly, Jr., and Dennis J. Koga				
7. PERFORMING ORGANIZATION NAME(S) AND ADDRESS(ES) Ames Research Center Moffett Field, CA 94035-1000			8. PERFORMING ORGANIZATION REPORT NUMBER A-962704	
9. SPONSORING/MONITORING AGENCY NAME(S) AND ADDRESS(ES) National Aeronautics and Space Administration Washington, DC 20546-0001			10. SPONSORING/MONITORING AGENCY REPORT NUMBER NASA TM-4762	
11. SUPPLEMENTARY NOTES Point of Contact: Robert A. Kennelly, Ames Research Center, MS 227-6, Moffett Field, CA 94035-1000; (415) 604-5860				
12a. DISTRIBUTION/AVAILABILITY STATEMENT Unclassified — Unlimited Subject Category 05			12b. DISTRIBUTION CODE	
13. ABSTRACT (Maximum 200 words) An F-104G aircraft at NASA's Dryden Flight Research Center has been equipped with a specially designed and instrumented test fixture to simulate surface imperfections of the type likely to be present near the leading edge on the wings of some laminar flow aircraft. The simulated imperfections consisted of five combinations of spanwise steps and gaps of various sizes. The unswept fixture yielded a pressure distribution similar to that of some laminar flow airfoils. The experiment was conducted at cruise conditions typical for business jets and light transports: Mach numbers were in the range 0.5–0.8, and unit Reynolds numbers were 1.5–2.5 million per foot. Skin friction measurements indicated that laminar flow was often maintained for some distance downstream of the surface imperfections. Further work is needed to more precisely define transition location and to extend the experiments to swept-wing conditions and a broader range of imperfection geometries.				
14. SUBJECT TERMS Laminar flow, Skin friction, Transition			15. NUMBER OF PAGES 36	
			16. PRICE CODE A03	
17. SECURITY CLASSIFICATION OF REPORT Unclassified	18. SECURITY CLASSIFICATION OF THIS PAGE Unclassified	19. SECURITY CLASSIFICATION OF ABSTRACT	20. LIMITATION OF ABSTRACT	